TECHNICAL UNIVERSITY OF LIBEREC
Faculty of Mechatronics, Informatics
and Interdisciplinary Studies

Manipulation of element distribution in laser-synthesized Pd/FeOx nanoparticles

Master thesis

Study programme: N0719A270001 – Nanotechnology
Study branch: N0719A270001NA – Nanotechnology

Author: **Bc. Sabrin Abdallah**
Supervisor: M.Sc. Rafael Omar Torres Mendieta, Ph.D.

Liberec 2022

TECHNICKÁ UNIVERZITA V LIBERCI
Fakulta mechatroniky, informatiky
a mezioborových studií

Řízení distribuce prvků laserem syntetizovaných Pd/FeOx nanočástic

Diplomová práce

Studijní program: N0719A270001 – Nanotechnologie
Studijní obor: N0719A270001NA – Nanotechnologie

Autor práce: **Bc. Sabrin Abdallah**
Vedoucí práce: M.Sc. Rafael Omar Torres Mendieta, Ph.D.

Liberec 2022

TECHNICKÁ UNIVERZITA V LIBERCI
Fakulta mechatroniky, informatiky
a mezioborových studií

Zadání diplomové práce

Manipulation of element distribution in laser synthesized Pd/FeOx nanoparticles

Jméno a příjmení:	Bc. Sabrin Abdallah
Osobní číslo:	M20000156
Studijní program:	N0719A270001 Nanotechnologie
Zadávající katedra:	Ústav nových technologií a aplikované informatiky
Akademický rok:	2021/2022

Zásady pro vypracování:

1. The general goal of the thesis is to study the influence of the pH in the manipulation over the element distribution of Pd/FeOx nanoalloys formed by reactive laser ablation in liquids (RLAL). As suggested one year ago by Prof. Tibbetts group and the recent results from the Torres-Mendieta group from our university, the critical point to manipulate the nanoalloy element distribution can be hidden in the superficial charge of the nucleating elements that would form nanoparticles. Thus, the natural answer to gain control over this is to manipulate the pH in the medium where RLAL occurs.
2. Another goal in this thesis is to gain information on the formation of either metal support interactions (MSI) or strong metal support interactions (SMSI) between the noble metal "Pd", and the metal oxide "FeOx". As proposed by the community interested in the synthesis of strong catalysts, such material combination can lead to the formation of SMSI, which can result in an outstanding catalytic performance due to the enhanced charge transfer between the elements or their geometrical disposition.
3. Finally, test the different physicochemical properties in the recently created nanoalloys. Understanding their chemical composition, morphology, surface charge, optical and magnetic response, among others, will help us to get a broader view of this material's reach and, thus, expand the perspectives for their exploitability in more applications.

Rozsah grafických prací:	dle potřeby dokumentace
Rozsah pracovní zprávy:	40-50 stran
Forma zpracování práce:	tištěná/elektronická
Jazyk práce:	Angličtina

Seznam odborné literatury:

[1] CALVO, Florent (ed.). Nanoalloys: from fundamentals to emergent applications. Newnes, 2013.
[2] ZHANG, Dongshi; Bilal; BARCIKOWSKI, Stephan. Laser synthesis and processing of colloids: fundamentals and applications. Chemical reviews, 2017, vol. 117, no 5, p. 3990-4103.
[3] FRIAS BATISTA, Laysa M., et al. Kinetic control of [AuCl4]- photochemical reduction and gold nanoparticle size with hydroxyl radical scavengers. The Journal of Physical Chemistry B, 2019, vol. 123, no 33, p. 7204-7213.
[4] JOHN, Mallory G.; TIBBETTS, Katharine Moore. Mechanism of nickel phyllosilicate formation by laser ablation in liquid. The Journal of Physical Chemistry C, 2020, vol. 124, no 24, p. 13273-13282.
[5] LIU, Jixing, et al. Deep understanding of strong metal interface confinement: A journey of Pd/FeO x catalysts. ACS Catalysis, 2020, vol. 10, no 15, p. 8950-8959.
[6] JOHN, Mallory G.; TIBBETTS, Katharine Moore. Controlling the morphology of copper-silica nanocomposites from laser ablation in liquid. Applied Surface Science, 2020, vol. 510, p. 145037.
[7] JOHN, Mallory G.; TIBBETTS, Katharine Moore. One-step femtosecond laser ablation synthesis of sub-3 nm gold nanoparticles stabilized by silica. Applied Surface Science, 2019, vol. 475, p. 1048-1057.
[8] BARCIKOWSKI, Stephan, et al. Handbook of laser synthesis of colloids. Universität Duisburg-Essen, 2016.
[9] ZHOU, Qi-Lin. Transition-Metal Catalysis and Organocatalysis: Where Can Progress Be Expected?. 2016.
[10] ASTRUC, Didier; LU, Feng; ARANZAES, Jaime Ruiz. Nanoparticles as recyclable catalysts: the frontier between homogeneous and heterogeneous catalysis. Angewandte Chemie International Edition, 2005, vol. 44, no 48, p. 7852-7872.
[11] WU, Peiwen, et al. Harnessing strong metal–support interactions via a reverse route. Nature communications, 2020, vol. 11, no 1, p. 1-10.
[12] RO, Insoo; RESASCO, Joaquin; CHRISTOPHER, Phillip. Approaches for understanding and controlling interfacial effects in oxide-supported metal catalysts. ACS Catalysis, 2018, vol. 8, no 8, p. 7368-7387.
[13] VAN DEELEN, Tom W.; MEJÍA, Carlos Hernández; DE JONG, Krijn P. Control of metal-support interactions in heterogeneous catalysts to enhance activity and selectivity. Nature Catalysis, 2019, vol. 2, no 11, p. 955-970.

Vedoucí práce	Dr. Rafael Torres Ústav nových technologií a aplikované informatiky
Datum zadání práce:	12. října 2021
Předpokládaný termín odevzdání:	16. května 2022

L.S.

prof.Ing. Zdeněk Plíva,Ph.D.
děkan

Ing. Josef Novák, Ph.D.
Vedoucí ústavu

V Liberci dne 19. října 2021

Declaration

I hereby certify that I have been informed that Act 121/2000, the Copyright Act of the Czech Republic, namely Section 60, Schoolwork, applies to my bachelor thesis in full scope. I acknowledge that the Technical University of Liberec (TUL) does not infringe my copyrights by using my bachelor thesis for TUL's internal purposes.

I am aware of my obligation to inform TUL on having used or licensed to use my bachelor thesis in which event TUL may require compensation of costs incurred in creating the work at up to their actual amount.

I have written my bachelor thesis myself using literature listed therein and consulting it with my supervisor and my tutor.

I hereby also declare that the hard copy of my bachelor thesis is identical with its electronic form as saved at the IS STAG portal.

Date:

Signature:

Abstract

The central theme of this thesis was to manipulate the element distribution in Pd/FeO_x nanoparticles (NPs) by modifying the existing methodology of reactive laser ablation in liquids (RLAL). The manipulation of the liquid medium's pH conditions composed of a Pd aqueous solution while ablating a Fe plate forced these elements to form phase-segregated nanoalloys. Moreover, these phases' composition, distribution, and morphology within the nanoalloy depended on the employed pH value. Unlike traditional nanoalloy synthesis alternatives, often limited to specific element combinations, forced employment of hazardous chemicals, and large chemical waste production, RLAL permitted tailoring designing the Pd/FeO_x nanoalloy system to a high degree; all this while suppressing potential detrimental environmental effects. In particular, the pH modification allowed the formation of Pd NPs encapsulating small FeO_x NPs, a type of phase-segregated structure known as nested NPs. It was also possible to form FeO_x NPs encapsulating nested Pd NPs, core-shell NPs comprising Pd as the core, and FeO_x as the shell, and small FeO_x NPs decorating the above. Such atypical morphologies also carried high-index facets, and as demonstrated by catalysis experiments, the combination of all these aspects suggests the formation of strong metal-support interactions (SMSI) between Pd and FeO_x. Since SMSI are one of the few tools able to improve the heterogeneous catalyst's response, the current findings leading to the catalytic response improvement of magnetophoretic motile Pd/FeO_x NPs through the formation of SMSI, are considered of striking importance for both; the laser-mediated generation of nanomaterials and the catalysis field. On the one hand, as clearly identified by the laser-synthesis community back in 2020, the major challenge in the field is the true control over nanoalloys composition; thus, the current findings push the field a step forward to gain complete control over the composition of nanoalloys. On the other hand, the method's versatility to exert the precise modifications leading to the formation of SMSI in magnetic nanocatalysts with the potential to be reused multiple times brings a refreshing hope for the field in terms of keep pushing the boundaries of customizing materials in benefit of the ever-increasing need of chemicals our society demands.

Keywords: nanoalloy, nanoparticle, iron, palladium, laser synthesis, femtosecond laser, reactive laser ablation in liquids

Abstrakt

Hlavním tématem této práce byla řízená distribuce prvků v nanočásticích Pd/FeO_x úpravou stávající metodiky reaktivní laserové ablace v kapalinách (RLAL). Úprava pH podmínek kapalného média složeného z vodného roztoku Pd při ablaci Fe plíšku přiměla tyto prvky k vytvoření fázově segregovaných nanoslitin. Navíc složení, distribuce a morfologie těchto fází v nanoslitině závisely na použité hodnotě pH. Na rozdíl od tradičních metod syntézy nanoslitin, které se často omezují na konkrétní kombinace prvků, nucené používání nebezpečných chemikálií a produkci velkého množství chemického odpadu, RLAL dovolila do značné míry přizpůsobení návrhu systému nanoslitin Pd/FeO_x při omezení potenciálně škodlivých vlivů na životní prostředí. Úprava pH umožnila tvorbu nanočástic FeO_x zapouzdřených ve větších nanočásticích Pd typu fázově segregované struktury známé jako vnořené nanočástice. Bylo také možné vytvořit FeO_x nanočástice zapouzdřující vnořené Pd nanočástice, nanočástice typu jádro-plášť obsahující Pd jako jádro a FeO_x jako plášť a malé FeO_x nanočástice zdobící výše uvedené. Tyto atypické morfologie vykazovaly fazety s vysokým indexem, a jak bylo prokázáno katalytickými experimenty, kombinace všech těchto aspektů naznačuje vznik silných interakcí kov-nosič (SMSI) mezi Pd a FeO_x. Vzhledem k tomu, že SMSI je jedním z mála nástrojů, kterými lze zlepšit odezvu heterogenního katalyzátoru, jsou současné poznatky vedoucí ke zlepšení katalytické odezvy magnetoforetických pohyblivých Pd/FeO_x nanočástic prostřednictvím tvorby SMSI považovány za velmi důležité jednak pro laserem zprostředkovanou generaci nanomateriálů, ale také pro oblast katalýzy. Na jedné straně, jak již v roce 2020 jasně identifikovala komunita zabývající se laserovou syntézou, hlavní výzvou v této oblasti je přesná kontrola nad složením nanoslitin. Současné poznatky tedy posouvají oblast o krok vpřed k získání úplné kontroly nad složením nanoslitin. Na druhou stranu, všestrannost metody pro provádění přesných modifikací vedoucích k vytvoření SMSI v magnetických nanokatalyzátorech s potenciálem opakovaného použití přináší naději pro tuto oblast, pokud jde o posouvání hranic pro přesné navržení materiálů ve prospěch neustále rostoucí potřeby chemikálií, které naše společnost vyžaduje.

Klíčová slova: nanoslitina, nanočástice, železo, palladium, laserová syntéza, femtosekundový laser, reaktivní laserová ablace v tekutinách

Acknowledgements

First and foremost, I would like to express my appreciation and gratitude to my supervisor Rafael Omar Torres Mendieta, Ph.D. for his utmost sincerity and kindness, for his unlimited advice, words of wisdom and support during this whole process. I also acknowledge that this work would not be possible without the help from the exceptional FEMTO-NANO team at the Institute for Nanomaterials, Advanced Technologies and Innovation that I am grateful to be a part of.

I would also like to acknowledge those who helped with characterizing my samples, namely, Dr. Dariusz Lukowiec for expanding my research with TEM, HR-TEM, SAED and EDX analysis, my kind colleague Ing. Ondra Havelka for ICP-OES measurements and help with carrying out the catalytic tests and Dr. Martin Cvek for the VSM analysis.

Last but not least, I would like to wholeheartedly thank my dear family and friends for their unlimited support and words of encouragement.

Contents

List of abbreviations

AP	**A**mino**p**henol
BSE	**B**ack **S**cattered **E**lectrons
CCD	**C**harge-**C**oupled **D**evice
demiH_2O	Demineralized Water
DLS	**D**ynamic **L**ight **S**cattering
EDX	**E**nergy-**D**ispersive **X**-ray Spectroscopy
EPMA	**E**lectron **P**robe at **M**icro**A**nalysis
HAADF	**H**igh **A**ngle **A**nnular **D**ark **F**ield
HRTEM	**H**igh-resolution **T**ransmission **E**lectron **M**icroscope
ICCD	**I**nternational **C**entre for **D**iffraction **D**ata
ICP-OES	**I**nductively **C**oupled **P**lasma-**O**ptical **E**mission **S**pectroscopy
LAL	**L**aser **A**ablation in **L**iquids
LDE	**L**aser **D**oppler **E**lectrophoresis
LFL	**L**aser **F**ragmentation in **L**iquids
LML	**L**aser **M**elting in **L**iquids
LSC	**L**aser **S**ynthesis of **C**olloids
MSI	**M**etal **S**upport **I**nteraction
NP	**N**itro**p**henol
NPs	**N**ano**p**articles
OM	**O**ptical **M**icroscopy
PLAL	**P**ulsed **L**aser in **A**blation in **L**iquids
PZC	**P**oint **Z**ero **C**harge
RLAL	**R**eactive **L**aser **A**blation in **L**iquids
SADP	**S**elected **A**rea **D**iffraction **P**attern
SAED	**S**elected **A**rea **E**lectron **D**iffraction
SE	**S**econdary **E**lectrons
SEM	**S**canning **E**lectron **M**icroscope
SMSI	**S**trong **M**etal **S**upport **I**nteraction
TEM	**T**ransmission **E**lectron **M**icroscope
UV-Vis	**U**ltraviolet-**V**isible
VSM	**V**ibrating **S**ample **M**agnetometry
WDX	**W**avelength-**D**ispersive **X**-ray Spectroscopy
XRD	**X**-ray **D**iffraction
ZP	**Z**eta **P**otential

List of Figures

List of Tables

1 Introduction

Since the well-known talk presented by Richard P. Feynman in 1959, the statement "There is plenty of room at the bottom" has struck a chord with scientists all around the world, making it a goal to push science forward and discover what we can achieve at the atomic scale [1]. Scientists have since developed instruments enabling us to study and even manipulate matter on that level. Thus, the nanotechnology field arose, which has evolved over the past two decades, and nowadays, nanostructures have become omnipresent and gained immense importance in our day-to-day lives. In fact, nanotechnology has secured its place in a myriad of important industry sectors, from materials and manufacturing, electronics, energy, and environment to life sciences and healthcare [2].

Similarly, an invention that has changed the way we construct the world is the laser, built in 1960 by Theodore Maiman, which, although initially criticized by skeptics, has gained undeniable importance in today's world. Maiman's invention was a stepping stone that led to the development of much more advanced lasers that have found applications everywhere, from the steel industry to medical clinics [3, 4]. Moreover, since the discovery made in 1993 by Fojtik and Henglein [5], that performing micromachining in the presence of liquids can allow the formation of extremely pure nanocolloids, it was possible even to envisage the laser-mediated manipulation of matter at the nanoscale. Hand in hand with the ability to observe and control matter at such dimensions, scientists are nowadays developing novel materials with tailored properties, functions, and potentially unique applications.

Taking inspiration from these exceptional advances, the current thesis aims to take a step forward in the laser-mediated synthesis of nanomaterials by manipulating the element distribution of phase-segregated nanoalloys. This goal is pursued by exploring the pH modification of the liquid environment when performing reactive laser ablation in liquids (RLAL). As the latest results from Tibbetts [6] and Torres-Mendieta groups point out [7], when employing laser-mediated synthetic approaches in liquids, the critical point to manipulating nanoalloys' element distribution can be hidden in the superficial charge of the nucleating elements that would form NPs. Thus, the natural answer to gain control over this is to manipulate the pH in the medium where RLAL occurs.

As such, this is a powerful concept; however, this thesis also aims to take the next step by investigating this idea's limits and prove if the element manipulation within a potent and recyclable catalyst like PdFe could lead to the formation of metal support interactions (MSI) or strong metal support interactions (SMSI). As very recently proposed by Liu et al. [8], such material combination can lead to the

formation of MSI/SMSI, resulting in an outstanding catalytic performance due to the enhanced charge transfer between the elements or their geometrical disposition. Thus, through this work, the reader will find an in-depth study of the performed endeavors to manipulate matter by laser radiation and, with this, contribute to the catalysis field, one of the fundamental pillars sustaining our society's accelerated lifestyle.

1.1 Nanomaterials

A nanomaterial can be classified as any material with at least one dimension below 100 nm. Initially, the term "nano" derives from a Greek word that translates to "dwarf", and this unit prefix represents a factor of 10^{-9}. Nanomaterials can take many different shapes and sizes, and according to the dimension of the materials, we distinguish 0D (e.g., spherical NPs), 1D (e.g., nanofibres, nanowires), 2D (e.g., nanocoatings, nanolayers), and lastly, 3D nanomaterials (e.g., nanofibrous layers). These materials possess unique properties compared to their bulk counterparts, for example, a high surface-to-volume ratio, which results from scaling the size of the material down to the nanoscale. This phenomenon leads to a higher surface area which enhances, among others, the materials' reactivity. Moreover, some metallic NPs exhibit high surface plasmon resonance which has potential application as sensors, e.g., gold [9, 10, 11] and silver NPs [12]. Due to their exceptional properties, nanomaterials have also found application in additional fields, such as medicine [13], tissue engineering [14], wound healing [15], electronics [16] and catalysis [17] among many others.

When it comes to NPs, there are many ways to synthesize them, such as using chemicals, synthetic or natural, or employing physical techniques. Generally, these methods fall into one of two approaches: the top-down or the bottom-up (Fig. 1.1). As the names suggest, NPs or nanostructures are produced by the break down of a bulk material in the top-down approach. Some methods that fall under this technique are high-energy ball milling [18], laser ablation [19], and chemical etching [20]. The bottom-up approach, on the other hand, utilizes reducing and stabilizing agents to build NPs from molecules, for example, by reducing metal salts using sodium borohydride [21]. This approach has been widely utilized because NPs of specific shapes and sizes can be synthesized by modifying the reaction conditions and precursor concentration. Needless to say, the possibilities of synthesizing NPs are endless. However, it is necessary to consider each approach's positive and negative aspects. For instance, using chemicals in the bottom-up approach allows the production of NPs with controllable size, but it also implies using harsh chemicals that can be toxic to the environment and the creation of by-products [22]. On the other hand, although most top-down strategies do not present such environmentally negative drawbacks, they still represent costly alternatives [23]. Thus, even when there are many nanomaterials with great potential applications, there is a need to develop cost-effective, easily reproducible, and ecologically respectful practices for more effective nanomaterials production that would be readily available. As the

reader will discover through the reading of the current work, the modification of RLAL proposed herein may bring such a long-awaited nanomaterials' synthetic answer.

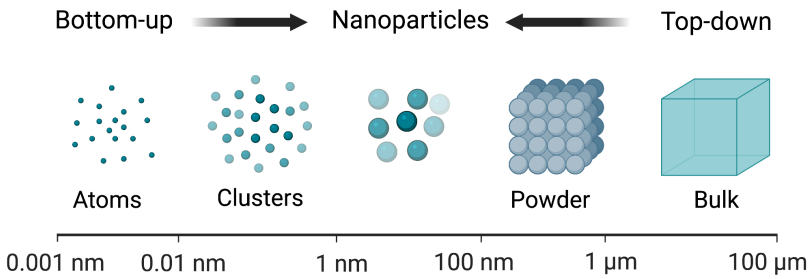

Figure 1.1: The two main approaches used in the synthesis of nanoparticles. Created in BioRender.

1.1.1 Nanoalloys

Nanoalloys are NPs composed of at least two metals, known as bimetallic nanoalloys. The tuning of the nanoalloys' composition, size, and element distribution enables controlling their physicochemical properties. They have gained significant importance, for example, in catalysis. The benefit of alloying two or more metals lies in the acquisition of new materials with enhanced properties compared to those of the monometallic NPs [24]. Thus, choosing the correct elements can lead to a synergistic effect where the alloy exhibits novel or unexplored properties. Alloying can, in some cases, also eliminate unwanted features, e.g., production cost, and at the same time, it can offer new properties, e.g., magnetic, which opens new possibilities in material sciences.

The structure of the nanoalloys can take on various forms (see Fig. 1.2). The most commonly discussed is the so-called core-shell structure, where one element constitutes the inner part (core) and the other, the nanoalloy's outer part (shell). This morphology type is specifically desired in catalysis; if one of the elements is a noble metal with high catalytic activity (e.g., Pd, Pt, Rh) and the other element posses, for example, magnetic response (Fe, Ni, Co) [25]. This can result in the construction of magnetophoretic motile catalysts, which can, among other things, save millions to the chemical industry by being reused multiple times when catalyzing chemical reactions [26]. Other nanoalloy structures with segregated phases include, for example, Janus, with metals' atoms divided into two equal parts, and sandwich nanoalloys. In the case of spherical NPs, the Janus morphology is given by two hemispheres consisting of the two elements separately. Moreover, a new nanoalloy morphology was recently synthesized, the so-called nested nanoalloy, where a smaller NP made of one element is nested in a larger NP made of the other element [27]. However, nanoalloys can also have mixed phases which can be either randomly or orderly distributed [28]. The randomly mixed nanoalloys are mostly recognized as solid solutions; thus, they exhibit no order. On the other hand, orderly mixed nanoalloys

have atoms structured in geometrical patterns, for example, a pattern of alternating planes of the two atoms.

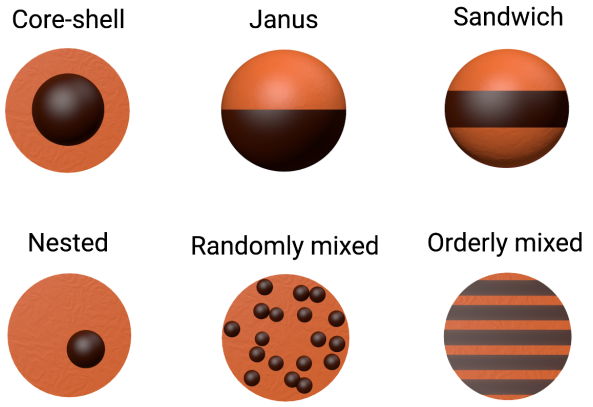

Figure 1.2: Various structures of bimetallic nanoalloys.

Thus, nanoalloys can find applications depending on their morphology, especially in heterogeneous catalysis. Namely, the choice of metals plays a crucial role in the overall catalytic performance. As previously stated, the key in alloying is to gain the benefits of both materials and possibly reduce their undesirable properties, e.g., chemical instability. In that case, the nanoalloy should contain one element that is catalytically active and an element that would support it and, in addition, enable the catalyst to be recycled. Such a combination can be found when alloying Pd, as the catalytically active component and Fe as the support and magnetically active component. Combining such materials can lead to the creation of metal-support interactions that are known to remarkably enhance the catalyst's performance [29].

The methods employed in the synthesis of such materials can play a crucial role in their final size, shape, and structure. Till now, most of the methods are based on wet chemistry, e.g., sol-gel [30] and coreduction [31]. Moreover, alternative physical methods have been employed as well, e.g., microwave-assisted synthesis [32], and thermal decomposition [33]. The generation of PdFe nanoalloys, in particular, has been achieved by cyanogel-derived synthesis of PdFe [34], continuous flow microwave synthesis of Pd supported on Fe_3O_4 NPs [35], chemical reduction [36] and wet impregnation [37].

Unlike these methodologies, the current thesis explores reactive laser ablation in liquids (RLAL), an actual method combining processes from wet chemistry and physical methods, which implementation conditions, also known as out-of-equilibrium, promise to produce nanoalloys, even from immiscible elements without the need of harsh chemicals. Further details can be found in section 1.3.

1.2 Catalysis

Catalysis is a necessary process involving the conversion of reactants into products in an energetically favorable way. This process is an integral part of our lives because we would not be able to function without substances like enzymes that catalyze most of the reactions taking place in our bodies. In the same way, the modern industry dramatically depends on catalysts; more than 90 % of reactions in the production of chemicals are catalyzed [38]. This means that the development of highly efficient catalysts is necessary for the catalytic field's advancement and societal advancement. In general, catalysts are substances that accelerate chemical reactions by lowering the activation energy, which results in the effective conversion of the reactants into the desired products, while catalysts are not consumed in the reactions [39]. The very first inspiration for producing such materials was found in nature by observing enzymes, which have a precisely tailored structure to catalyze a given reaction [40]. Thus, with this in mind, scientists begin aiming to develop novel catalysts that mimic the properties of enzymes. As a result, NPs, which have a large room for tailor design, have proven to be suitable catalysts in many reactions [41].

Catalysis can be divided into two types: homogeneous and heterogeneous [42]. Homogeneous catalysis is the term used when the catalyst is in the same phase as the reactants, e.g., a soluble catalyst in a solution. Although it is nearly impossible to separate the catalyst from the solution due to high solubility, this allows for higher performance. In contrast, heterogeneous catalysis is based primarily on solids, like metals, being the catalyst in a reaction where the precursors are in a different phase. Metal-based NPs, in particular, have been widely used in heterogeneous catalysis given their unique properties, like their high surface area, which provides more active sites responsible for modifying the kinetics of a reaction [43]. One thing that has been observed about the NPs size and the catalytic performance is that with the decreasing size of the NPs, there is an increase in the number of surface sites per unit weight of metal which generally leads to more active catalysts [44]. However, these sites can be deactivated by the reactants and, thus, hinder the catalytic activity [45]. Nevertheless, some of the undesirable properties of a catalyst can be overcome by using a support.

1.2.1 MSI, SMSI

Metal-support catalysts have long been studied due to their high catalytic performance and wide range of applications in heterogeneous catalysis (e.g., CO oxidation, CO_2 hydrogenation, Fischer-Tropsch reaction)[47, 46]. The thing that is most studied is the metal-support interaction (MSI), which mainly depends on the charge transfer, chemical composition, interfacial perimeter, NPs morphology, and strong metal-support interaction (SMSI) [48]. The metal part commonly consists of noble metal NPs, e.g. Au, Pt, Pd [49, 50], and the support is usually an oxide (TiO_2, SiO_2, Al_2O_3)[51]. The support stabilizes the metal NPs (e.g., against leaching, thermal stability) and ensures uniform distribution of catalytically active sites [44, 52] or, as Coq describes in his work, the support acts as a supramolecular ligand [53].

Metal-support interactions and their modifications can play an essential role in designing catalytic systems with improved performance. There are multiple ways to tune metal-support interactions. As Van Deelen et al. suggest, control of MSI can be done by either modifying the individual catalyst's components (the metal and the support) or by modifying the final composite material [48]. Modifications of both-the metal and the support- can be achieved by choosing a proper chemical composition. In the metal case, tuning can also be achieved by controlling the particle's size. In comparison, modifications of the support include changes in morphology, doping, and surface modification. Thus, the extent of the MSI modifications depends on the type of metal as well as the support and on the different approaches of preparation and activation of the catalysts [53].

As a part of metal-support interactions, SMSI plays a crucial role in determining catalytic activity, and stability [48]. The term "strong metal-support interaction" was first mentioned in an article by Tauster et al. [54], where this phenomenon was identified due to the decreased capability of H_2 and CO chemisorption by group VIII metals supported on TiO_2 [55]. SMSI is mainly identified at the metal-support interfaces where the support is a reducible oxide, such as TiO_2, CeO_2, and Fe_2O_3 [48]. Reducible oxides are able to exchange oxygen quite easily because the lowest empty energy states available consist of cation d-orbitals that lie not too high above the valance band. Their bandgap is relatively low (< 3 eV) compared to that of nonreducible oxides (SiO_2, Al_2O_3). The oxygen removal creates excess electrons (oxygen vacancies), which are distributed on the empty cation levels, therefore, causing a shift in their oxidation state (from M^{n+} to $M^{(n-1)+}$). [51]

1.2.2 Mechanisms of SMSI

There are multiple mechanisms involved in the formation of strong metal-support interaction. According to numerous studies, the major effects that result from the formation of the SMSI are the electronic, and the geometric effect [46, 53, 56].

Electronic effect

When discussing strong metal-support interaction, what is meant by the electronic effect is the charge redistribution at the interface between the metal and the support. These electronic interactions are driven by fundamental principles of energy minimization and continuity of electric potential in a solid [46]. Electron transfer takes place at reactive interfaces, where chemical bonds are broken and new ones are formed. The local charge redistribution involves a few atomic layers at the interface. Depending on the type of metal-support system, SMSI can cause pronounced changes in the electronic properties.[46]

As previously mentioned, the types of oxides used in the production of SMSI alter the electronic effect. Nonreducible oxides (with no transition metals) have cations with no d-orbitals available for bonding; thus, the cations favor interacting with the anion (oxygen), and consequently, that leads to a weak bond between the metals and the support (SiO_2, MgO, ZrO_2)[50, 46]. Whereas in the case of reducible oxides,

the surface cations (transition metals) with d-orbital electrons can easily interact with the supported metal (e.g. Pd/TiO_2 [57], Pt/Fe_3O_4 [58]). A study[59] done on Pt/TiO_2 system showed there is an overlap between the metal atom and the cation's d-orbital electrons contributing to a weak covalent bond. However, the main interaction was found to be ionic, which was due to the electron transfer from the reduced cation to the adjacent metal atom. The loss of surface anions means the reduction of surface cations by acquiring d-orbital electrons, thus facilitating the electron transfer to the metal. Moreover, surface defects of the oxide support, such as vacancies, accumulate electrons, leading to an increased electron density on the supported metal. According to studies, there is a direct correlation between the electron transfer and the electronic structure of the reducible oxide as well as the size of the metal clusters.[46]

Geometric effect

The geometric effect is usually thought of as the initial meaning of SMSI [54]. It involves the mass transfer of suboxide species to the metal, thus covering the metal clusters partially (decorating) or fully (encapsulating) (Fig. 1.3). This effect is driven by the minimization of the high surface energy of the metal NP by the suboxide species which are generated from the support under reductive conditions. Metals with high surface energy that are able to activate hydrogen are susceptible to encapsulation; therefore, reducible oxides are required to generate the suboxide species [50]. The suboxide coverage of the NP consists of a few atomic layers [48, 60]. Although extensive coverage of the metal NP is shown to have a detrimental effect on the catalytic activity caused by the blockage of active sites, the suboxides can act as Lewis acids by changing the electronic structure on the metal's surface, hence promoting the activation of reactants and enhancing the catalytic activity [48].

In order to study the encapsulation mechanism, Fu et al. [57] proposed a two-step mechanism that leads to the encapsulation of the metal. Firstly, it is necessary for the interstitial cation, Ti^{n+} (n=3 or 4) in this case, to transfer close to the metal-support interface. As for the second step, the encapsulation requires the surface energy γ of the metal (Pd) to be greater than that of the support (TiO_2). Therefore this mechanism is also driven by the principle of energy minimization. Generally, metals with surface energy above 2 J/cm^2 are more susceptible to encapsulation [46]. Apart from the surface energy, it is suggested that the encapsulation also depends on the work function [61]. Multiple studies also showed the size dependence of the metal NPs broadly relates to the SMSI [60]. Du et al. [62] studied the size effect on SMSI of Au NPs supported on TiO_2 and discovered that larger Au NPs are more likely to be encapsulated than smaller ones. Similarly, Zhang et al. [63] reported that SMSI between Au and TiO_2 depends on the size of Au NPs, as well as on TiO_2 facets. SMSI is more likely to be formed by ca. 5 nm large Au NPs and by TiO_2 {001} and {100} facets.

One of the most recent and exceptional works on studying the SMSI done by Wu et al.[64] describes an alternative way of producing SMSI by a so-called reverse

route. This new approach intends to expand the boundaries of the conventional SMSI formation strategies that require high-temperature treatment and ultimately lead to an uncontrollable encapsulation process resulting in a limited exposure of active sites. Wu et al. proposed that the encapsulation should create a thin layer permeable to small molecules in an ideal scenario while still preventing the dissolution, disintegration, and aggregation of active sites during catalysis. In this work, fully encapsulated Pd-Fe_3O_4 core-shell NPs were treated under a reductive atmosphere to achieve an intermediate state (porous structure) that allows partial exposure of active (metal) sites. The study revealed that Pd atoms migrate into the Fe_3O_4 lattice forming strong interactions, and that, along with the formation of SMSIR, a partial electron transfer from Pd to Fe_3O_4 occurs.

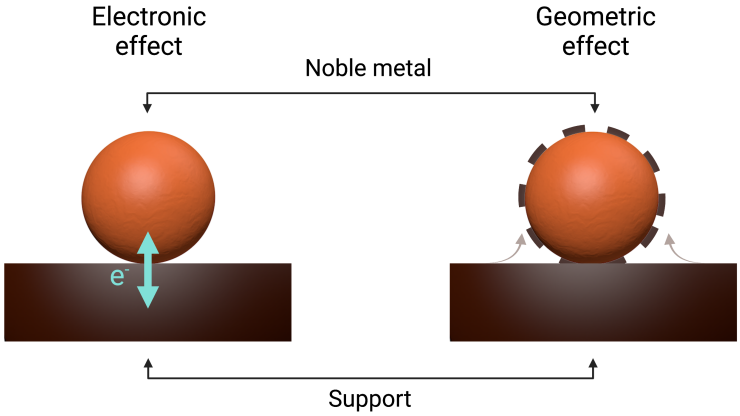

Figure 1.3: The two major effects resulting from the formation of a strong metal-support interaction (SMSI): the electronic and the geometric effect. Created in BioRender.

1.3 Laser synthesis of colloids

As scientists, we have the social responsibility to develop safer and lower waste-producing processes for the production of nanomaterials [65]. From this perspective, the interactions between light and matter have brought various appropriate alternatives, among which, laser synthesis of colloids (LSC) is gaining increasing attention due to its versatility, safeness, and applicability [66]. In this synthetic practice, a laser is employed to reduce the size of a bulk material immersed in a liquid to the nanometer regime, which causes the synthesis of extremely pure and elementally-controlled NPs that can reach sizes from 1-100 nm. As such, LSC is a general term used to describe many different laser-mediated synthesis approaches, e.g., pulsed laser ablation in liquids (PLAL), laser melting in liquids (LML), and laser fragmentation in liquids (LFL). Each of these methods yields different products, so in order to achieve the desired results, one has to choose the laser-irradiation parameters carefully [66, 67]. For instance, in the case of PLAL, the appropriate irradiation

conditions can allow the ablation of a solid target immersed in a liquid environment leading to the generation of NPs, or can allow the ablation accompanied by the liquids' optical breakdown, which can cause the molecular dissociation of the liquid. This, in turn, can lead to the formation of radicals that may react with the recently synthesized NPs modifying their chemical structure [68]. In the case of LML and LFL, the irradiation conditions can lead to the heating, melting, evaporation or even explosion of micro or NPs dispersed in liquids, allowing the creation of NPs with controlled size [69, 70].

Although the materials processing by laser radiation has been around directly after the laser invention, it was used to structure surfaces, and the material detached from those surfaces was regarded as waste [71]. It was until 1993 that in a gold processing experiment in water, Fojtik and Henglein realized that such waste was actually staining the water with a red color [5]. This is how they realized that the "waste" was, in fact, ultrapure Au NPs, opening in that way a nobel and very vibrant field, which due to its versatility, is believed to become the top practice towards the development of increasingly complex nanostructures.

1.3.1 Types of lasers

The type of laser used in LSC can drastically affect the process and results. There are two main types of lasers used: continuous-wave (cw) and pulsed lasers. The cw lasers generate coherent and high-energy electromagnetic waves continuously, whereas the pulsed lasers release energy in packages during a specific amount of time (operation time), at a specific repetition rate, and pulse duration. Aside from delivering the radiation in confining windows of time, thanks to methodologies like Q-switching or mode-locking, among others, every pulse carries massive amounts of energy being the peak power in each pulse; the clearest example of this:

$$P_{peak} = \frac{P_{avg}}{f_{rep}\tau} \tag{1.1}$$

Where, P_{avg} represents the average power of a laser, f_{rep} is the repetition rate at which the pulses are delivered, and τ is the pulse width. Thus, even when there are very powerful cw lasers, from eq.1.1 it is evident that the shorter the pulse width, the higher the peak power reached in each pulse, being enough to exceed the most powerful cw counterparts. Pulsed lasers can therefore achieve higher peak powers and are more efficient in removing matter from a solid surface than cw lasers [72].

Moreover, in the case of cw lasers, the energy is continuously delivered to the target, where it is accumulated until it overcomes the threshold energy of the material, and at last, material melting followed by evaporation is achieved. This process is not effective in LSC because on the one hand, the interaction between cw radiation and matter leads to energy propagation throughout the atomic lattice in the form of heat, and on the other hand, prolonged light exposure can lead to evaporation of the liquid medium and thus affect the ablation rate. Ideally, a pulsed laser is preferred for LSC, as in the case of PLAL, where it is possible to deliver a great number of photons in fractions of seconds with no significant energy accumulation

enhancing in this way, the material detachment from the area confined to the laser beam's irradiation spot [66].

Three types of lasers are used in LSC, namely, nanosecond (ns), picosecond (ps), and femtosecond (fs) lasers, which, as the name suggests, vary in pulse duration. The most inexpensive out of the three is the nanosecond laser, but it is also the least efficient and can cause unwanted heat transfer in the material. The picosecond laser allows a high repetition rate without causing significant heat transfer, but at the same time, this quality can lead to bubble shielding. Lastly, the femtosecond laser is the most efficient as well as the most expensive, but the high-energy laser beam can also cause bubble shielding and optical breakdown [66].

Last but not least, it is important to highlight that, although the current production rate record set by Streubel et al. [73] at few g/h is still far from the scalability to industrial processes, the latest advances in laser designing promise to turn LSC into the future of high-quality NPs design.

1.3.2 Principles of PLAL

Upon irradiation of a bulk target by a focused pulsed laser beam in a liquid medium, the photons confined in the pulse are absorbed by the electrons at the superficial target's atoms. Since the pulses can confine a massive amount of photons in windows of time shorter than the electronic recombination time (ps), the electrons can absorb a large number of photons in a non-linear optical process known as multi-photon absorption. Since the electrons keep absorbing photons without going back to their basal state, they finally get released from their atomic system in a process known as multi-photon ionization. As a single pulse can exert such processes in a multitude of electrons, all released electrons end up forming an electronic cloud above the initially irradiated area. Since this electronic cloud leaves behind a large number of ions, the interaction between both contrasting charged areas results in the formation of a quasi electrostatic field, which, when its energy surpasses the target's cohesive energy, leads to the target's explosion, known as the Coulomb explosion (see Fig. 1.4).

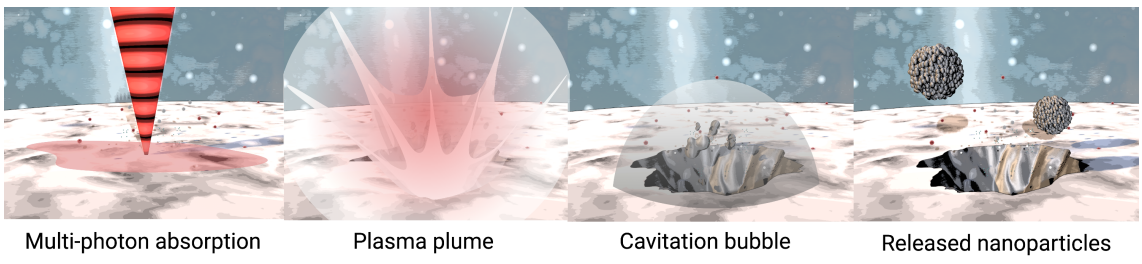

Figure 1.4: Pulsed laser ablation in liquids (PLAL) principle from the first step of multi-photon absorption to the release of NPs from the cavitation bubble.

This explosion liberates colossal energy and leads to the ejection of various species like ions, atomic systems, and electrons. All these species form a hot plasma encapsulated by the liquid medium, which keeps detaching material from the initially

irradiated zone by transferring kinetic energy in the form of electronic collisions to the remaining atomic systems and to the surrounding liquid interface dissociating the most proximal liquid molecules. The whole process lasts only a few ns, and when the plasma extinguishes, it transfers its remaining energy to the surrounding liquid that didn't dissociate. However, as the transferred energy is not enough to keep dissociating the surrounding liquid molecules, it only transforms them from the liquid to gas state. Since such gas is created in the surroundings of a relatively cold liquid, it gives rise to a cavitation bubble where all the former plasma species find the perfect conditions to nucleate, forming NPs.

The cavitation bubble lasts for a few ms and afterward collapses, creating a fluid micro-jet ejecting all the recently formed NPs into the liquid medium. Once the still hot NPs get in contact with the liquid medium, which is in a lower energy state, the energetic contrast at the interface between the liquid and the NPs surface detonates a surface tension phenomenon resulting in the re-shaping of the NPs into spheres, thus, resulting in the formation of a nanocolloid [74]. As the reader can infer from the described process, the principal aspects controlling the final NPs composition are hidden in the irradiation conditions, the employed solid target, and the liquid medium. The current thesis is especially devoted to exploring the liquid medium, which, as described back in 2015 by Matsumoto at al. [75], opens an almost limitless exploration gap because the species that form the liquid can even control the physicochemical characteristics of the produced NPs; thus, giving rise to laser ablation in liquids while chemical reactions occur, i.e., RLAL.

1.3.3 Reactive laser ablation in liquids

RLAL is a novel method employed to generate a wide range of nanoalloys by combining the PLAL approach and photochemical reduction. This method is based on irradiating a solid target immersed in a metal salt solution (Fig. 1.5). The irradiation process is similar to that of PLAL; the plasma formed at the laser focus produces the dissociation of the liquid molecules surrounding it, and depending on the liquid nature, different types of radicals can be created. However, the presence of the salt dramatically changes the conditions and alters the basic process of PLAL; the reactive species generated enable the reduction of the metal salt. Subsequently, the reduced species can interact with the species obtained from the ablation of the target and lead to the formation of nanoalloys [76]. The alloying can occur in the plasma; however, it is primarily promoted in the cavitation bubble and the bubble-liquid interface. Usually, ps-/fs-lasers are employed in this method because by modifying the laser's peak intensity; we are able to gain control over the plasma's density and, ultimately, the NPs' size distributions [68]. Moreover, as lately suggested by Tibbetts group [6], by modifying the pH of an aqueous solution, it could be possible to gain control over the element distribution in the final nanoalloy.

The precise timescales of reactions occurring during RLAL depend predominantly on the laser source used [6]. For example, by employing a ns-laser to produce RLAL in an aqueous solution, the plasma cools for about 1 μs after irradiation, the cavitation bubble forms in the range of 0.1–1 μs and collapses over the range of

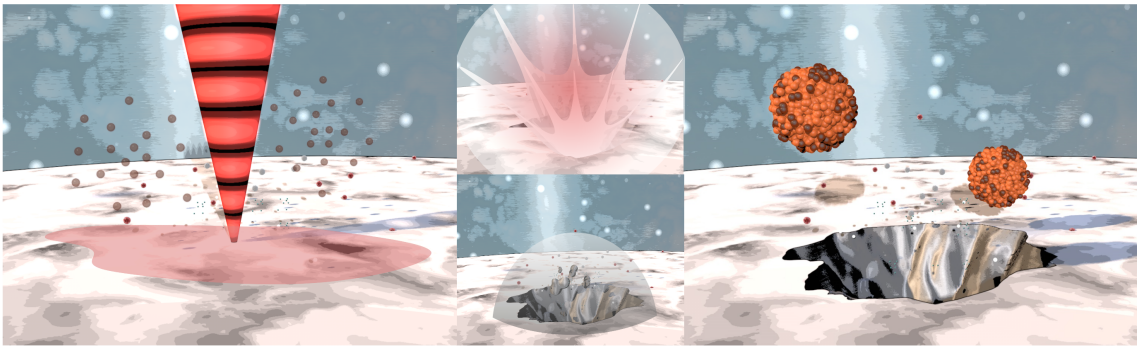

Figure 1.5: Reactive laser ablation in liquids (RLAL) process generating bimetallic nanoalloys.

several hundred microseconds. However, when employing a fs-laser, the timescales of reactions succeeding the laser pulse are as follows: cavitation bubble is formed in about 100 ns, within the range of several hundred fs to a few ns, free electrons are generated and hydrated at the target-water interface where they react with dissolved species from the solution to form the metal atom nuclei. Moreover, hydrogen peroxide is generated within about 10 ns which reacts with the newly formed metal species leading mainly to the production of large isolated metal NPs. Around 100 ps the target's surface is also subjected to reactions in which the ejected atoms and liquid droplets oxidize and merge to react with the residual metal salt and the nuclei. Finally, it is suggested that the low salt concentration at the target-water interface is responsible for the generation of ultra-small NPs stabilized by the ablated target material. Note that the reactive species in the example mentioned above (solvated electrons, OH radicals, or H_2O_2) belong to an aqueous solution, i.e., the involved reactive species will depend on the employed liquid, and with this, the different reactions leading to the formation of nanoalloys. Yet, since the driving idea of the current thesis is that the simple pH modification of a solution is enough to control the element distribution within the nanoalloys, it was necessary to employ water as the selected solvent. Thus, the example mentioned above is significant for this thesis work.

2 Proposition

Here we propose the possible mechanism involved in producing FePd nanoalloys by RLAL when modifying the pH of the salt solution.

Since the employed material consists of Fe foil and Pd salt dissolved in water, the predominant Pd species thought to interfere in forming FePd nanoalloys are reduced Pd ions and dissolved Pd salt anions. These species can react with those ejected from the Fe foil in the cavitation bubble and at the bubble-liquid interface as follows:

$$Pd^{2+} + Fe = Pd + Fe^{2+} \tag{2.1}$$

$$Fe + 2H_2O = Fe^{2+} + 2OH^- + H_2 \tag{2.2}$$

$$Fe + Pd = FePd \tag{2.3}$$

Based on the miscibility and surface energies of Pd and Fe, their alloying should enable the production of phase-segregated nanoalloys according to the Hume- Rothery rules [77]. In addition, considering that the solvent can play a crucial role in the final morphology, it is expected that the phase-segregated type of morphology our nanoalloys can adopt will be a core-shell, where the shell should be composed of the element most prone to oxidation. Even though eq. 2.1 suggests that Pd would comprise the shell given that the Fe ions would serve as a means for its reduction; in this case, Fe would preferentially compose the shell due to the surface segregation of the Fe atoms. Furthermore, the reason behind influencing the NPs' morphology by modifying the pH of the solution in RLAL was only recently proposed by Mukherjee and co-workers [78]. Thus, an additional equation must be added to the previously mentioned when considering the pH modification:

$$Fe + 2H^+ = Fe^{2+} + H_2 \tag{2.4}$$

This reaction indicates that by lowering the pH, and thus, increasing the concentration of hydrogen protons $[H^+]$, the oxidation of Fe is enhanced, which results in the reduced amount of Fe in the NPs, permitting Pd to be the dominant element and, with this possibly occupying the nanoalloys' shell. On the other hand, when the $[H^+]$ is decreased, the oxidation of Fe is prevented, which enables it to be integrated into the final nanoalloy, making it the dominant element within the nanoalloys, enhancing its chances of forming the shell (Fig. 2.1). Moreover, as 0.1

mM metal salt solution is reported to be the optimum concentration allowing for the production of core-shell NPs with a partially filled shell[7], then it is expected that when Fe forms the shell, the NPs released into the water after the collapse of the cavitation bubble consists of a catalytically active Pd core and a partially filled Fe shell which undergoes oxidization. Being this morphology ideal for the generation of the SMSI effect, thus, resulting in highly efficient recyclable catalysts. In summary, making the pH modification of the Pd aqueous solution an ideal practice leading to the element distribution control within phase-segregated nanoalloys, which can result in the formation of SMSI.

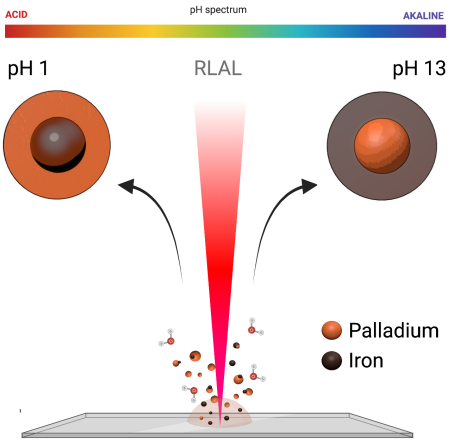

Figure 2.1: The proposed influence pH modification has on the element distribution in the final FePd nanoalloy synthesized using RLAL. Sketch created in BioRender.

3 Methodology

3.1 Materials

The reagents employed in the current thesis are potassium tetrachloropalladate(II) (>98% K_2PdCl_4, Sigma-Aldrich, USA), hydrochloric acid (35%+ HCl, Penta Chemicals Unlimited, Czech Republic), potassium hydroxide (≥99.95% KOH, Sigma-Aldrich, USA), iron foil (≥99.99% Fe, Sigma-Aldrich, USA), 4-nitrophenol (≥99% 4-NP, Sigma-Aldrich, USA), sodium borohydride (≥98.0% $NaBH_4$, Sigma-Aldrich, USA), and demiH_2O (18.2 MΩ·cm).

3.2 Sample preparation

In a glass vial, 0.1 mM aqueous solution of K_2PdCl_4 was prepared and placed in an ultrasonic bath (SONOREX DIGITEC DT 510 H, BANDELIN, Germany) to dissolve completely. Later, the pH of the Pd salt solution was measured using a pH meter (InLab Routine Pro-ISM, Mettler Toledo, USA) and a corresponding amount of HCl or KOH aqueous solution was added to modify the pH (see Tab. 3.1). The pH of the unmodified Pd salt solution was, on average, 3.64 ± 0.06.

Sample	unmodified pH	Acid/base amount	modified pH
pH 1	3.555	8.43 mL$^{(a)}$	1.177
pH 3	3.706	300 μL$^{(b)}$	2.990
pH 3.6	3.656	-	-
pH 5	3.525	115 μL$^{(c)}$	5.300
pH 7	3.592	150 μL$^{(c)}$	7.346
pH 9	3.650	186 μL$^{(c)}$	8.865
pH 11	3.615	1010 μL$^{(c)}$	10.755
pH 13	3.695	0.3 g$^{(d)}$	12.689

Table 3.1: Summary of the amount of acid/base added to the Pd salt solution (unmodified pH) and the resulting modified pH which is in accordance with the name of the samples. $^{(a)}$0.8M HCl aqueous solution, $^{(b)}$0.09M HCl aqueous solution, $^{(c)}$5.6 g/L KOH aqueous solution, $^{(d)}$ ≥99.95% KOH.

The amount of acid or base needed to modify the pH of the Pd salt solution

accordingly was calculated using the following formula:

$$M_1V_1 + M_2V_2 = M_3(V_1 + V_2) \tag{3.1}$$

Where M_1 is the molarity of the acid/base, V_1 is the volume of the acid/base solution needed to change the pH, M_2 is the molarity of the prepared Pd salt solution, V_2 is the corresponding volume and M_3 is the sought-after molarity, also known as the concentration of $[H^+]$ protons, which can be calculated from the formula below (eq. 3.2). It is important to note that the actual amount of acid/base added to the Pd salt solution was higher than the theoretical amount calculated.

$$M = 10^{-pH} \tag{3.2}$$

$$[H^+][OH^-] = 10^{-14} \tag{3.3}$$

Laser ablation of the Fe foil immersed in the as-prepared Pd salt solution with modified pH was carried out by an industrial femtosecond pulsed laser (Onefive Origami XP-S, NKT Photonics, Denmark) operated at an average output power of 5.1 W, a repetition rate of 1 MHz, pulse duration 400 fs, a central wavelength of 1030 nm with a spectral bandwidth < 5 nm, and an output beam of 5 mm at the width of $1/e^2$. Therefore, the foil was irradiated at its ablation threshold (5 μJ).[79]

The laser beam was focused and moved throughout the surface of the Fe foil by a scanning system composed of a two-axis galvanometer scanner head (intelliSCAN 14, SCANLAB, Germany), and an F-theta lens (f = 160 mm). The irradiation took place while the foil was immersed in 40 mL of the Pd salt solution in a 60 mL glass dish. The foil was set to be 3 mm below the liquid-air interface so that the high absorption of the infrared laser light by the water molecules was prevented. Moreover, a magnetic stirrer was placed inside the dish to disperse the forming NPs and avoid reirradiation (see Fig. 3.1). Finally, the velocity of the laser scanning head was set to the maximum speed of 2 m/s to avoid the cavitation bubble's shielding, frequently resulting in NPs productivity reduction.

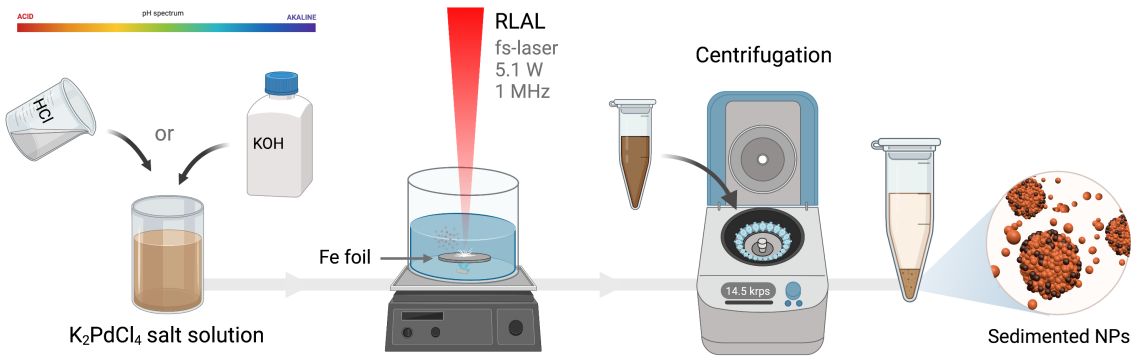

Figure 3.1: Preparation of Pd/FeO_x NPs using RLAL. Mixing of reactants, laser irradiation of the Fe foil in the presence of the Pd salt solution, and cleaning samples by centrifuging. Created in BioRender.

After the irradiation process was complete, the samples‘ pH was recorded to verify that its value did not vary. Later, the samples were centrifuged (Centrifuge MiniSpin plus, Eppendorf, Germany) in 2 mL Eppendorfs for 10 min at 14,500 rpm. This enabled the separation of the NPs from the supernatant composed of the Pd salt residue. After the supernatant was taken out from the Eppendorf, the missing volume was replaced by the uncleaned sample. These steps were repeated until all NPs in the solvent were totally separated from the liquid residues. Lastly, to obtain clean NPs, the Eppendorfs were filled with demiH_2O and homogenized in an ultrasonic bath. For the catalysis experiments, the samples were later dried overnight in an oven at 65 °C.

3.3 Pollutant degradation screening

The catalytic transformation from 4-NP to 4-aminophenol (4-AP) was used to test the catalytic activity of the Pd/FeO_x NPs. This model reaction involves the 4-NP catalytic hydrogenation, where $NaBH_4$ is the hydrogen donor and the NPs the catalyst. The NPs role as a catalyst consists of serving as a support for the transformation reaction by adsorbing the $NaBH_4$ and 4-NP over their surface, facilitating a 6-electron powered reaction. In brief, the first pair of electrons in junction with an H^+ serves to reduce 4-NP to a nitroso compound, which reduces to its corresponding hydroxylamine by the second electrons pair and $2H^+$; finally, this is reduced to 4-AP by the last electrons pair together with an H^+. The transformation reaction was monitored by inspecting the absorbance decrease of the 4-nitrophenolate at 401 nm using a UV-Vis spectrophotometer (DR 3900, Hach Lange, USA) [7].

For the catalytic tests, 48 μL of 5mM 4-NP, 240 μL of 0.1M $NaBH_4$, along with one of the four different concentrations of the NPs (1.48, 3.01, 6.20, 13.23 mg/L) and demiH_2O were placed in a 2ml Eppendorf. The reactants were briefly mixed using a vortex before the mixture was transferred to a quartz cuvette and placed into the UV-Vis spectrometer (Fig. 3.2). The absorbance was measured for 5 mins at 401 nm.

Due to the excess of $NaBH_4$ added to the reaction, the hydrogen source could be considered constant, and therefore, the catalytic transformation from 4-NP to 4-AP followed a pseudo-first-order reaction kinetics. Hence, the reaction rate constant (k_{app}) can be easily determined through the following equation:

$$ln\left(\frac{C_t}{C_0}\right) = ln\left(\frac{A_t}{A_0}\right) = -k_{app}t \tag{3.4}$$

Where C_t/C_0 represents the ratio of phenolate ions at any time of the reaction, A_t/A_0 is the ratio of their absorbance at 401 nm, and by plotting these values as a function of time, we obtain the k_{app} as the slope value. Moreover, the total efficiency of the Pd/FeO_x catalyst, determined by the activity parameter (κ_c), can be calculated from the slope value of the linear regression of k_{app} as a function of the catalyst concentration [80].

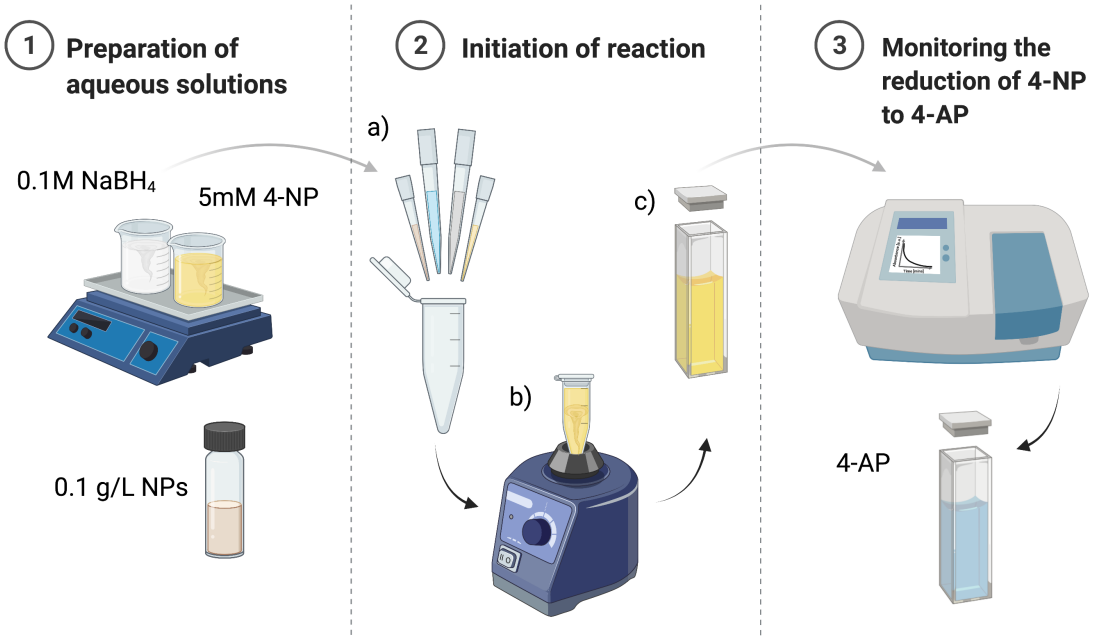

Figure 3.2: Catalytic test procedure for 4-NP degradation. The preparation of $NaBH_4$, 4-NP and Pd/FeO_x NPs aqueous solutions (1), addition of all reactants into a single Eppendorf (2a), homogenization (2b) and transfer of the mixture into a quartz cuvette (2c) for the monitoring of 4-NP degradation (3). Created in BioRender.

4 Characterization techniques

Various characterization techniques were used to fully understand the synthesized nanomaterial's physicochemical properties. Many crucial aspects need to be addressed when characterizing the prepared NPs to attribute functions to the structures. For example, it is necessary to gain information about the stability of the NPs, the size distribution, morphology, element distribution, and concentration, among many others (Fig. 4.1).

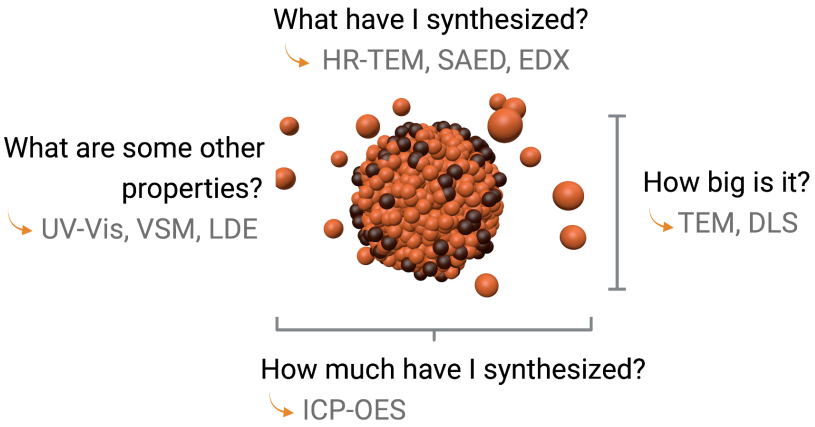

Figure 4.1: Illustration of NPs, multiple questions that arise while trying to understand them and the methods employed in this work to characterize them.

In this work, ultraviolet- visible (UV-Vis) spectroscopy was used to inspect the samples' optical properties and observe the absorbance of the material based on its concentration (for example, in the pollutant degradation screening). Dynamic light scattering (DLS), as well as transmission electron microscopy (TEM), were used to determine the NPs size, hydrodynamic size in case of DLS, and real size in case of TEM. The stability of the nanocolloids was determined using laser doppler electrophoresis (LDE), employing the same instrument used for DLS. Moreover, high-resolution TEM (HR-TEM) also allowed us to obtain information about the NPs morphology and the element distribution when combined with a detailed analysis of the d-spacings. Both, selected area electron diffraction (SAED) and energy-dispersive X-ray spectroscopy (EDX), enabled the determination of element distribution in the samples. Furthermore, inductively coupled plasma-optical emission

spectroscopy (ICP-OES) was employed to identify the concentration of the samples. Lastly, to gain information about the magnetic properties of the NPs, the samples were characterized using vibrating sample magnetometry (VSM).

4.1 UV-Vis spectroscopy

The analysis was carried out by a UV-Vis spectrophotometer (DR3900, Hach, USA) with wavelengths ranging from 320 - 1100 nm and a resolution of 1 nm. This spectrophotometer uses light in the visible and adjacent regions produced by a halogen lamp to interact with a sample in transmission mode. Before the light reaches the sample, it goes through a monochromator, employing a set of diffraction grids and filters to separate and select the light according to the different wavelengths (Fig. 4.2). Depending on the range of wavelengths, the light passes through and interacts with the sample placed in a cuvette one wavelength at a time. A photodetector then detects the transmitted light, the signal is processed, and the instrument gives us the absorbance as a function of wavelength at last.

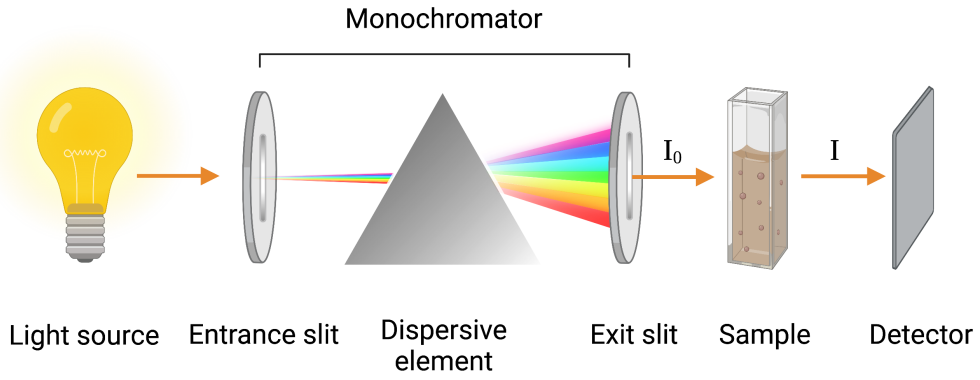

Figure 4.2: Basic principle of a UV-Vis spectrophotometer enabling the analysis of a colloidial sample. Created in BioRender.

The instrument measures the intensity of the transmitted light (I), and compares it to the initial intensity of the light generated from the halogen lamp (I_0). This value represents the transmitance (T_λ), which is usually given in percentages. Therefrom the absorbance is calculated as follows:

$$A = -log_{10}(T_\lambda) = -log_{10}(\frac{I}{I_0}) = \frac{ln(e^{\alpha(\lambda)d})}{ln(10)} = \frac{\alpha(\lambda)d}{2.3} \tag{4.1}$$

Where λ is the wavelength, α is the absorption coefficient, and d is the optical path length (the internal width of the cuvette containing the sample).

According to the Beer–Lambert law, the absorbance of a solution is directly proportional to the concentration of the absorbing species and the path length (eq.

4.2). Hence, for a given path length (d), we can determine the concentration of the species (c) , e.g. nanolloys, in our solution.

$$A = \epsilon_\alpha c d \tag{4.2}$$

Moreover, by combining UV-Vis spectroscopy analysis with the Mie theory calculator, a physicomathematical theory describing the scattering of electromagnetic waves by spherical particles, we can estimate the size and structure of the nanoalloys. However, some conditions must be satisfied, e.g. the sphericity and homogeneity of the particles and the planarity of the light waves. The NPs interaction with light can then be described using the following formulas [76]:

$$C_{ext} = \frac{24\pi^2 R^3 \epsilon_d^{3/2}}{\lambda} \frac{\epsilon''_m}{(\epsilon'_m + 2\epsilon_d)^2 + (\epsilon''_m)^2} \tag{4.3}$$

$$\epsilon'_m = \epsilon^\infty - \frac{\omega_p^2}{\omega^2 + \gamma^2} \tag{4.4}$$

$$\epsilon''_m = \frac{\omega_p^2 \gamma}{\omega(\omega^2 + \gamma^2)} \tag{4.5}$$

$$\gamma = \frac{\nu_F}{L_{bulk}} \tag{4.6}$$

Where C_{ext} represents the NPs extinction coefficient, R their radius and ϵ_d the dielectric function of the NPs, ϵ_m the dielectric function of the solvent, ϵ^∞ the dielectric function at high frequencies (for most materials it is equal to 1), ω represents the frequency of the incoming light, ω_p the frequency at which the electrons in the NPs resonate with theque incoming light, ν_F the Fermi velocity (from the Fermi energy) and L_{bulk} the pathway of electrons in the bulk material.

The necessary homogeneity assumption for this equation is much more challenging to meet for multi-metallic NPs such as nanoalloys. Nevertheless, the Mie theory can be used to consider particular types of multi-metallic NPs, e.g., core-shell structure [81]. In such a case, the eq. 4.3 transforms to

$$C_{ext} = 4\pi R^2 m \times Im \left\{ \frac{(\epsilon_{shell} - \epsilon_m)(\epsilon_{core} - 2\epsilon_{shell}) + (1-g)(\epsilon_{core} - \epsilon_{shell})(\epsilon_m + 2\epsilon_{shell})}{(\epsilon_{shell} + 2\epsilon_m)(\epsilon_{core} + 2\epsilon_{shell}) + (1-g)(\epsilon_{shell} - 2\epsilon_m)(\epsilon_{core} - \epsilon_{shell})} \right\} \tag{4.7}$$

Where ϵ_{shell} represents the dielectric function of the material located at the shell side, g the shell's volume fraction, ϵ_{core} the dielectric function of the material located at the core, and as in the previous set of equations, R represents the particles' radius and ϵ_m the solvent's dielectric constant. Note that if $g = 0$, the eq. 4.7 reduces to the eq. 4.3 representing a NP without a shell. Therefore, the final spectrum hides information not only about the particle size and composition, but also about the element distribution in the particles together with the shell and core diameters.

Although this is a very appealing technique providing very useful information, it is still essential to keep in mind that due to its statistical nature, it is essential

to combine the information extracted from it with complementary characterization methods discussed in this chapter.

4.2 DLS

The DLS measurements were carried out by a DLS measurement system (Zetasizer Nano ZS90, Malvern Instruments Ltd., UK) with the laser's wavelength centered at 632.8 nm, and were employed to assess the NPs hydrodynamic size and stability.

The measurement is based on detecting scattered electromagnetic waves upon interaction with spherical particles (ranging from about 0.3 to 5000 nm) dispersed in a solvent (Fig. 4.3). When the light is scattered from all particles present in the colloid, the electromagnetic waves interfere with each other randomly and create a speckle pattern, which is detected by a photodetector and transformed into a signal. Due to the Brownian motion, however, the particles are not still, and thus, the speckle pattern changes through time, resulting in the fluctuation of the measured light intensity. The intensity of the scattered light depends on the size of the particle; the larger the particle is, the more light it scatters, and the less the intensity fluctuates. A correlation curve is constructed by comparing intensity fluctuation at different time intervals. Proportional to the exponential rate decline of the correlation curve is the diffusion coefficient (D), which is directly related to the particle's size through the Stokes-Einstein equation (eq. 4.8).

$$D = \frac{k_b T}{6\pi\eta r} \tag{4.8}$$

Where k_b represents the Boltzmann's constant, T the temperature of the medium, η the viscosity of the medium and r the particles' size.

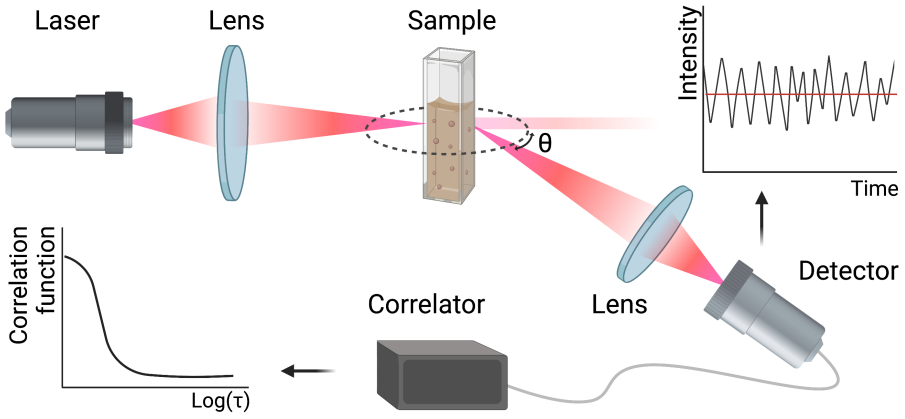

Figure 4.3: Principle of a DLS measurement. Created in BioRender.

4.2.1 LDE

Another method that uses DLS is LDE, which measures the electrophoretic mobility of NPs present in a sample. The LDE system employs the same instrument used for DLS. However, a special cuvette is used in this case, which contains two electrodes attached to it that send an electrical current through the sample. The charged species move to the electrodes at different rates depending on the voltage applied. From the measured velocity, known as the electrophoretic mobility, we can obtain the Zeta potential (z) of the sample from Henry's equation (eq. 4.9).

$$z = \frac{3\eta\mu_E}{2\epsilon f(\kappa\alpha)} \tag{4.9}$$

Where η is the viscosity of the medium, μ_E the electrophoretic mobility, ϵ the dielectric constant of the analyzed material, and $f(\kappa\alpha)$ Henry's function, which value is either 1.5 or 1.0. The value 1.5 is employed to measure medium-sized particles dispersed in an aqueous medium (this is known as the Smoluchowski approximation). The 1.0 value is used for small particles dispersed in a low dielectric constant medium (this is the Huckel approximation).

The knowledge of Zeta potential (ZP) allows us to understand the stability of the particles. The magnitude of ZP is attributed to the degree of electrostatic repulsion between akin particles in close proximity. A high ZP (negative or positive) indicates that the particles will resist aggregation and thus be electrically stabilized, while a low ZP means the particles will tend to aggregate and eventually sediment. As agreed by convention, $|0mV| > z > |5mV|$ leads to a poor stability, $|10mV| > z > |30mV|$ incipient stability, $|30mV| > z > |40mV|$ moderate stability, $|40mV| > z > |60mV|$ good stability, and $z > |61mV|$ excellent stability [82].

4.3 HR-TEM

The TEM images were acquired by a scanning transmission electron microscope (FEI, TITAN 80-300, ThermoFisher Scientific, USA) working at 300 kV, and were employed to extract the NPs size, which was assessed by fitting a log-normal curve to the values of 700 NPs counted manually.

Unlike optical microscopy (OM), which is based on the interaction of electromagnetic waves with a sample, electron microscopy uses the interaction of an electron beam with a sample to produce an image. According to the de Broglie relationship evidencing the wave-particle duality of electrons, the electrons' wavelength can be described by the following formula:

$$\lambda = \frac{h}{mv} \tag{4.10}$$

Where h is the Planck's constant ($6.626 \cdot 10^{-34}$ J·s), m is the mass of an electron ($9.1 \cdot 10^{-31}$ kg), and v its velocity. Since the electrons shall be accelerated in an electron microscope to interact with the sample, their velocity can be described in terms of the microscope's accelerating voltage in the following form:

$$eV = \frac{1}{2}mv^2 \tag{4.11}$$

Where e is the charge of an electron ($1.6 \cdot 10^{-19}$ C), and V is the accelerating voltage (300 kV in our situation). Thus, by replacing this electron velocity in the eq. 4.10, it is possible to get the final form of the electrons wavelength:

$$\lambda = \frac{h}{\sqrt{2meV}} = 2.24\, pm \tag{4.12}$$

Moreover, since the velocities of electrons in a microscope get close to the speed of light, the electrons suffer relativistic effects, namely, length contraction, time dilation, and increase in mass, thus, eq. 4.12 transforms to:

$$\lambda = \frac{h}{\sqrt{2meV}} \cdot \frac{1}{\sqrt{1 + \frac{eV}{2mc^2}}} = 1.96\, pm \tag{4.13}$$

Since the resolution of a microscope comes from the wavelength of the employed radiation, it is evident that the electron microscope able to reach 1.96 pm must have a better resolution than conventional optical microscopes limited by the wavelength of light (400-700 nm). Given this outstanding resolution, we are able to view objects as small as a few nanometers and, in the case of HR-TEM, down to the atomic scale.

There are two main types of electron microscopes, namely, scanning (SEM) and transmission (TEM) electron microscopes. The samples in this work were characterized using TEM (HR-TEM) because it enables high-resolution imaging and the possibility of determining crystallographic families based on d-spacing analysis.

Generally, the electron microscopes operate on similar principles, where primary electrons are generated from an electron gun in the head of the microscope. The source can be a hot cathode (usually a tungsten filament or a single LaB_6 crystal) or an auto-emission source. Due to the high voltage applied ($\sim$ 100–300 kV), the electrons are emitted from the source. The highly accelerated primary electron beam then enters a system of condensing lenses where it is focused on a desired spot size and location on the sample.

Primary electrons interact with matter to generate various signals. Some of the electrons are transmitted, some are absorbed, and others are scattered (Fig. 4.4). Each of these interactions provides different type of information. We then choose the corresponding signal based on what we want to study. For example, in SEM, the main signals studied are the secondary (SE) and the back-scattered (BSE) electrons, which give information about the topography and atomic number based on the topographical and chemical contrast. In TEM, on the other hand, the signals studied come from the transmitted electrons that are detected by a charge-coupled device (CCD) camera at the bottom of the chamber.

TEM requires a very thin sample ($\sim$ 100 nm) for the electrons to be transmitted through it. To obtain high-quality images, it is thus necessary to prepare the sample with high precision. Even though the CCD camera has high resolution ($<$ 0.1 nm), the final image quality greatly depends on the sample preparation. When analyzing

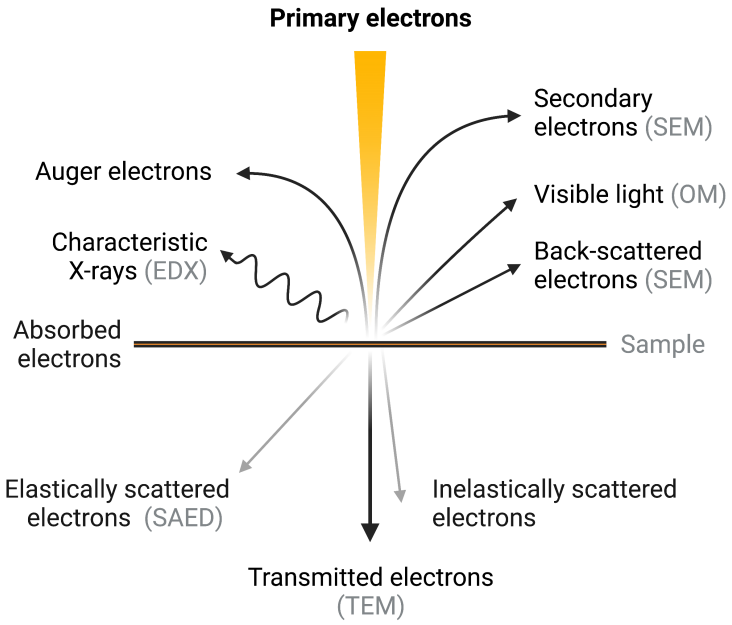

Figure 4.4: Types of electron-matter interactions and the corresponding technique used to analyze the sample based on the detected electrons.

a colloid, the sample is prepared by depositing a droplet of the sample on a copper grid covered by a carbon film to avoid overcharging, and letting it dry before placing the holder into the instrument.

4.3.1 SAED

SAED measurement can be carried out in the same TEM instrument from which TEM images are obtained. Moreover, SAED enables the analysis of especially small areas, e.g., an area with one or more NPs. Considering that SAED is employed to analyze the crystallinity of materials, the precision and the ability to select areas makes SAED more accurate in analyzing samples with a lower concentration of NPs than, for example, X-ray diffraction (XRD), where the area analyzed is much larger.

The sample is the same as for the TEM analysis. Hence, the highly focused primary beam of electrons interacts with the matter, as previously mentioned (Fig. 4.4). The interaction can be understood as an interaction of an electromagnetic wave of the primary electron with an electron of a fixed atom in the sample. This interpretation occurs because the accelerated electrons have an extremely short wavelength (10^{-3} nm) and the average d-spacing in the lattice is much larger (10^{-1} nm). Therefore, the diffraction of an electron on an atom from an atomic plane of a crystal lattice is possible if Bragg's law (eq. 4.14) is satisfied.

$$n \cdot \lambda = 2d \cdot sin(\theta) \tag{4.14}$$

Where n represents the refractive index of the material, λ the wavelength of electrons, d the distance between the atoms, and θ the angle between the primary

electron beam and the atomic plane.

The diffracted electrons are detected by a high-angular annular dark field detector (Model 3000, Fischione Instruments Inc., USA). Therefrom we obtain a selected area diffraction pattern (SADP) in which the bright spots are a result of a constructive interference of electrons satisfying Bragg's law, and the black background corresponds to destructive interference. Depending on the crystallinity of the material the SADP varies. For example, in the case of a monocrystalline sample, the SADP consists of points of a square grid and concentric rings in the case of a polycrystalline sample. We can determine which crystallographic families are present in the sample from these patterns.

4.3.2 EDX

Electron probe microanalysis (EPMA) is a non-destructive spectroscopic method used to identify the chemical composition of a sample. This method is based on the detection of X-rays that the sample emits. EPMA enables qualitative, semi-quantitative, and quantitative element analysis at very small "spot" sizes using an energy-dispersive (EDX) or wavelength-dispersive (WDX) X-ray spectrometer. These spectrometers are usually a part of either SEM or TEM.

In EPMA, the sample is irradiated by an accelerated and highly focused beam of electrons. If the energy of the primary electrons is high enough, they can eject electrons from the sub-valence electron shell of the sample's atoms. As the excited atom returns to the ground state, an electron from a higher energy level fills the vacancy of the ejected electron by releasing a quantum of energy in the form of X-rays. These X-rays are characteristic of each element, and thus, by knowing the energy or wavelength of these rays, we can identify the elements present in a sample [83].

The electrons from higher energy levels can fill vacancies in multiple ways. The energy levels are named alphabetically $K, L, M, N, ...$ and the corresponding electron transitions between them $\alpha, \beta, \gamma, ...$ where α is the transition from the closest neighboring level, β is the transition from the second closest level, γ the third and so on (Fig. 4.5). For example, if a vacancy in the energy level K is filled by an electron from the adjacent level (L), then the transition is called K_α.

In the case of EDX, the X-rays are detected by a semiconductor (e.g. Si(Li) or Ge) and generate an electron-hole pair (in our case, the employed detector was an energy-dispersive X-Max 80 from Oxford Instruments, UK). The current that is produced in the detector is proportional to the energy of the incoming rays. The generated signal is then directed to a multichannel analyzer that analyzes the electrical impulses and creates a whole energy spectrum of the X-rays in the form of a histogram.

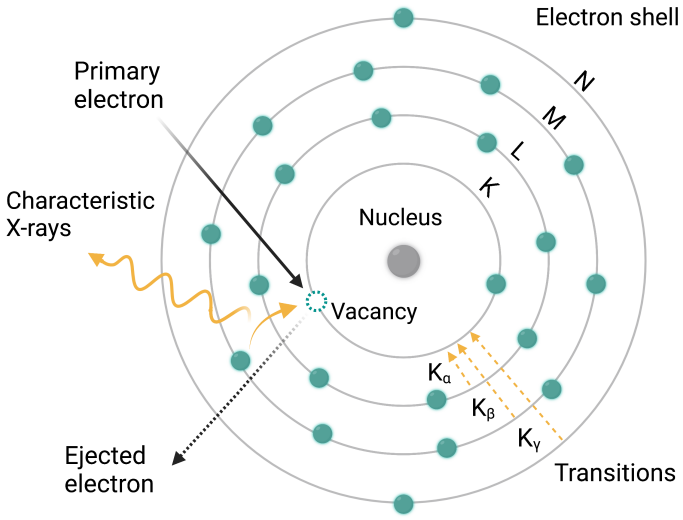

Figure 4.5: Illustration of the electron shell and the transitions taking place upon excitation by primary electron beam in EDX analysis.

4.4 ICP-OES

In an ICP-OES instrument, the sample, transformed into a homogeneous solution by a chemical digestion process, is continuously injected into a nebulizer, where it forms an aerosol. The species present are then excited due to the collisions with the Ar plasma, which is maintained by an alternating high-frequency magnetic field at extremely high temperatures (6000 - 10000 K). To return to the ground state, the excited species release energy in the form of photons with a characteristic wavelength corresponding to the specific element according to the following equation:

$$\Delta E = h\nu = \frac{hc}{\lambda} \tag{4.15}$$

Where ΔE represents the energy difference between the excited electronic level and the ground level, h the Planck's constant that has a value of $6.626 \cdot 10^{-34}$ Js, ν represents the frequency of the emitted electromagnetic wave, λ its wavelength, and c the velocity of light in the vacuum with an average value of $3{\cdot}10^8$ m/s.

Subsequently, an optical spectrometer detects the intensity of the emitted photons, which is proportional to the number of atoms present in the analyzed volume. Our samples were analyzed by an ICP-OES spectroscope (Optima 2100Dv, Perkin Elmer, USA) with a detection limit of 0.2 ppb, enabling us to understand how many elements composed our nanoalloys. Thus, helping us to determine the nanoalloys element composition. Furthermore, the data obtained were converted to atomic percentages (at.%) to understand better the sample's composition based on the amount of the present elements.

4.5 VSM

To measure the magnetization using a VSM instrument, the sample is mounted to a vibrating holder that oscillates in a system of coils. Due to the sample's magnetization, the oscillation induces a voltage on the coils, which can be measured and transformed into a hysteresis loop, permeability, or magnetic moment. The hysteresis loop (Fig. 4.6), in particular, gives information on the saturation magnetization (M_s) representing the maximum magnetic moment per unit volume within the sample, remanence magnetization (M_r) defining the magnetization remaining in the sample after turning off the applied external magnetic field, and coercivity (H_C) denoting the magnetic field's intensity required to reduce material's magnetization to zero. Moreover, using this information, it is possible to assess the remanent ratio (R)= M_r/M_S, which tells how easy it is to reorient the direction of magnetization after removing the magnetic field. This is of particular interest for selecting the appropriate application for the studied material; for instance, a high remanent ratio can be handy for magnetic recording, and a low one for motor cores or transformers minimizing the energy dissipation with alternating fields [84]. In addition, these values also enable calculating the anisotropy constant (K) within the samples, referring to how the magnetic properties can be modified depending on the samples' orientation. This is calculated according to the Stoner–Wohlfarth theory [85].

$$K = 1.02 \cdot H_C \cdot M_S \tag{4.16}$$

In the current thesis work, the NPs were analyzed using a VSM (Model 7404, Lake Shore, USA) in a magnetic field of ± 15 kOe at ambient conditions. The samples were inserted into a VSM sample holder (730931 Kel-F, powder upper/bottom cup) mounted on a fiberglass tail with a vibration frequency of 82 Hz, employing a vibration amplitude of 1.5 mm, and time constant of 100 ms.

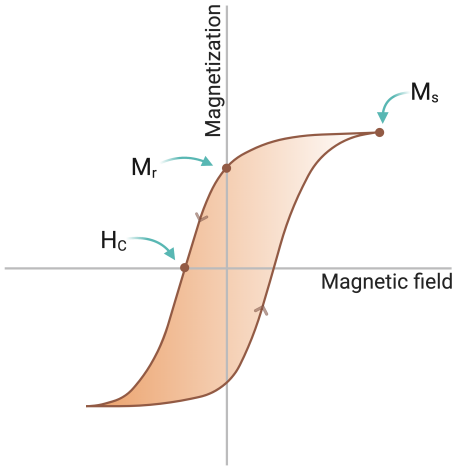

Figure 4.6: Illustration of a hysteresis loop obtained from VSM with defined points corresponding to the saturation (M_s), remanence (M_r), and coercivity (H_C) of a ferromagnetic material.

5 Results and discussion

5.1 Morphology

As observed in Fig. 5.1A, the most significant difference between the samples' absorbance lies in their decline. While samples created using larger pH values exhibit a more straight absorbance decrement, those created employing a lower pH tend to show a more pronounced one. According to the Mie theory [81], such behavior corresponds to the one of nanoalloys with phase segregation, in particular, to core-shell NPs. Such an observation largely agrees with the Hume-Rothery rules stating that two elements cannot form substitutional alloys if; (i) their atomic radius differs by more than 15%, (ii) their crystal structures are not similar, and (iii) they have different valency, and electronegativity [77]. In the current case, although Pd and Fe have a coincident crystalline structure (face-centered cubic) and at least one coincident valency value (2) [86], the rest of the rules are violated, i.e., the difference between Pd radius (163 pm) and Fe radius (126 pm) is 29.36% , according to the following equation:

$$Difference\% = \left(\frac{r' - r''}{r''}\right) \times 100\% \leq 15\% \tag{5.1}$$

Where r' represents the atomic radius of the first element and r'' of the second one. Moreover, the electronegativity of both elements largely differs (1.8 for Fe and 2.2 for Pd) [86]. Thus, it is expected to obtain a phase-segregated type of structure such as a core-shell. In addition, the samples' absorbance spectra provide further information about the element distribution within the NPs; as observed in Fig. 5.1B, the most significant decline corresponds to a larger amount of Pd within core-shell NPs where the Pd composes the core and Fe the shell, i.e., Pd@Fe NPs. Oppositely, a less pronounced decrease corresponds to Pd@Fe NPs where the Pd composing the core is less abundant. Note that the experimental data is not entirely coincident with the theoretical calculation obtained employing the open access Mie calculator from Prof. Lucien Saviot ([87]), which considers the nanoalloys are spherical, have a mono-modal size distribution, and the element distribution is the same for all particles. In an actual synthetic procedure, such ideal conditions are rarely satisfied, and thus, the calculated graphs can provide minimal information about the morphological properties found in the produced nanomaterials. This is why it is mandatory to employ complementary methodologies to unveil our nanoproducts' real aspect and properties.

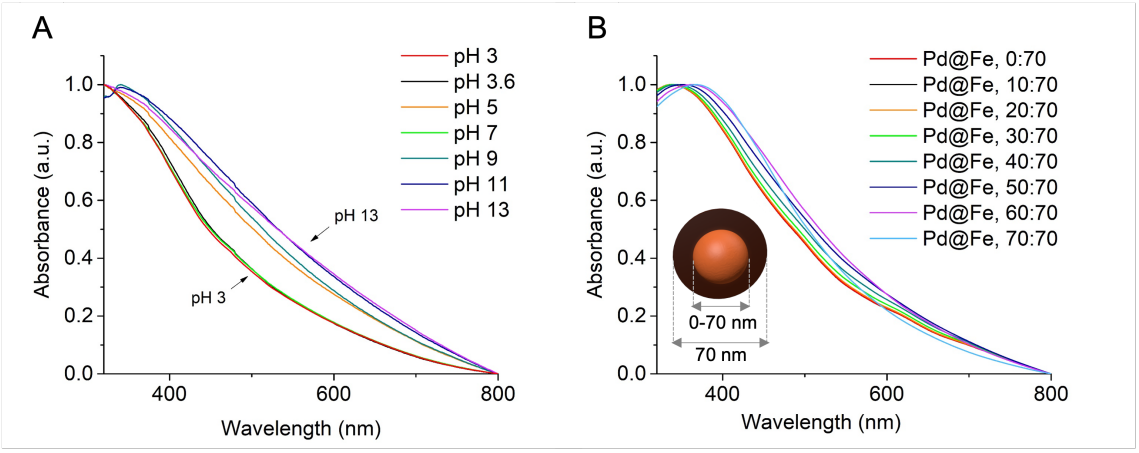

Figure 5.1: Absorbance spectra of A) prepared samples employing various pH conditions, and B) set of simulated graphs considering Pd@Fe NPs are dispersed in water. The considered total NPs size is 70 nm, also representing the shell diameter, and the core's size varies from 0 to 70 nm. Thus, the notation 0:70 corresponds to NPs purely composed of Fe, 40:70 to NPs with a core diameter of 40 nm and a shell of 70 nm, and 70:70 to NPs entirely composed of Pd. Note that the sample where pH 1 was employed could not be measured. When keeping the sample in a colloidal form, the highly acidic conditions digested the solid NPs, making their measurement in a colloidal form impossible.

5.1.1 Shape and size

TEM

As observed in Fig. 5.2, the pH conditions primarily affect the NPs composition, shape, and size. The different contrast degrees within the samples suggest that all NPs present phase segregation as predicted by their absorbance spectra, although not entirely the core-shell type of segregation. Since transmitted electrons generate bright-field TEM images, either superposition of NPs or heavier element composition can result in the observed darker color. Thus, very loaded images such as the ones belonging to pH 3.6, 5, or 11 could be misleading due to the large number of superposing NPs. However, the rest undeniably show that within single NPs, it is possible to observe different darkness degrees; thus, phase segregated composition. On the other hand, their shape is similar in all cases, i.e., quasi-spherical. As explained in Chapter 1.4, in a classical LAL experiment, NPs ejected from the cavitation bubble's collapse are still hot when released into the liquid medium; thus, their interaction with the solvent's cold molecules increases the NPs surface tension resulting in their reshaping into spheres. Differently, in RLAL, the solvent is full of metal salts causing the additional effect of salt reduction over the NPs surface, thus, leading to the formation of quasi-spherical particles. In addition, the NPs size is unique; although wide, most samples show a monomodal distribution, which is not typical for classical LAL, but has been observed multiple times in RLAL [78]. As described by Gokce and Zhigilei groups back in 2018 [88], the NPs bimodal size

distribution is a consequence of two effects, the nucleation and growth of small particles in the cavitation bubble and the rapid ejection of bigger pieces beyond the cavitation bubble. Thus, if the particles coming from the cavitation bubble keep growing due to the reduction of metal salts over their surface, it is expected that they will reach a monomodal size distribution.

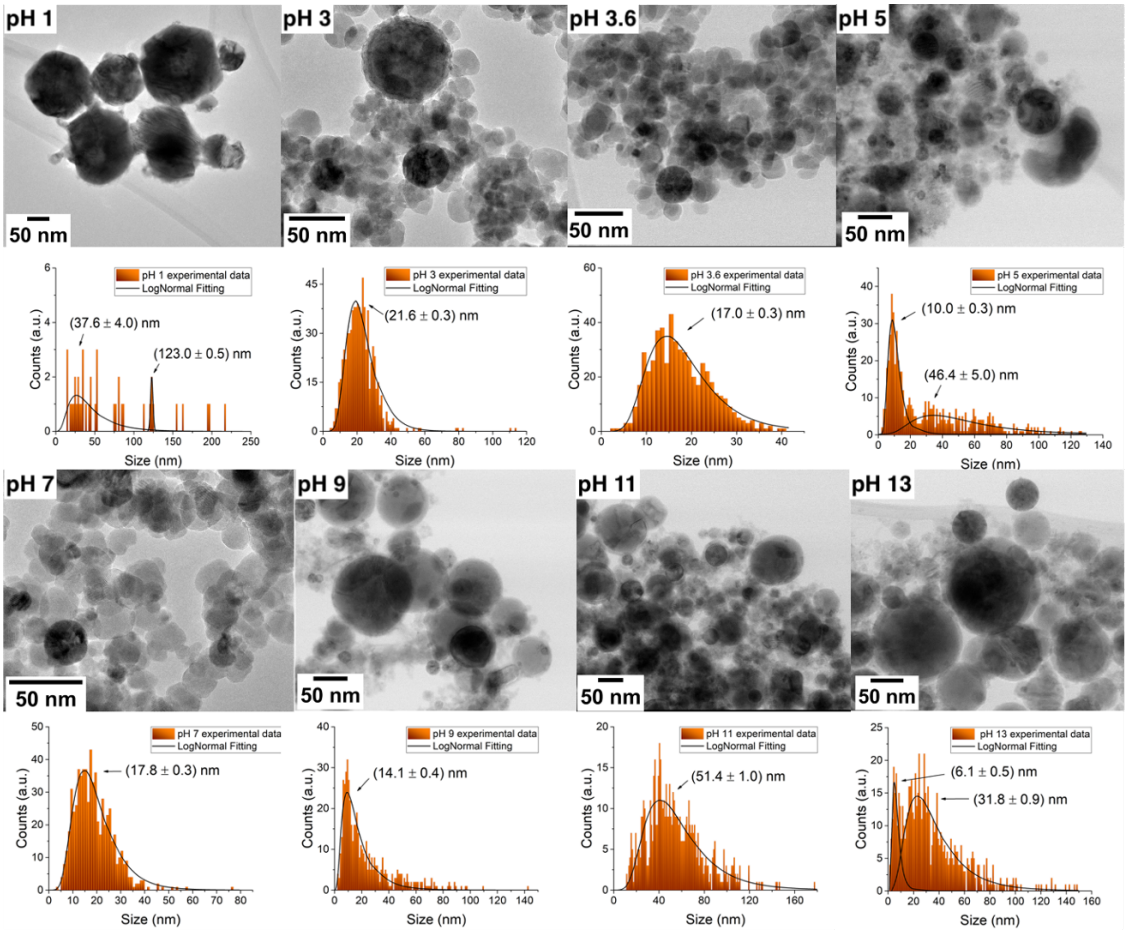

Figure 5.2: TEM images of synthesized Pd/FeO_x NPs and the corresponding size histograms with log-normal fitting.

A deeper inspection indicates that NPs synthesized at pH 1 have a peculiar morphology, where large and dark NPs seem to encapsulate small and light NPs, thus creating phase-segregated NPs that have been recently identified as nested NPs [89]. Considering Pd is a heavier element than Fe, it is plausible that we are forming Pd NPs with nested Fe in them. Moreover, the irregular but similar to the rest of the samples, quasi-spherical shape seems to indicate the formation of high-miller index facets; however, such analysis will be presented in the subsection corresponding to element distribution. The samples corresponding to pH 3–13 present a different type of element segregation, which agrees with our prediction from the UV-Vis results, i.e., the contrast difference within individual particles seems to indicate that either we are creating isolated Pd and Fe NPs, or small Fe NPs start to cover the surface of big Pd NPs partially. Moreover, when the pH value increases, it is easier

to find Pd@Fe NPs, yet always accompanied by small Fe NPs decorating the surface, especially in the case of samples produced using pH 5 and 9 that show the most significant number of small NPs. This morphology is highly desired for heterogeneous catalysis, given the presence of MSI sites, as mentioned in Chapter 1.2. The presented results are in accordance with the hypothesis presented in Chapter 2. Thus, we prove here that by varying the pH of the Pd salt solution, we can favor the formation of geometrical structures that can potentially present MSI sites.

DLS

The measurements obtained using the DLS instrument help assess the particles' hydrodynamic size, yet, such information can be expressed in various forms: based on intensity, volume, and number. As discussed in Chapter 4, the DLS instrument measures the fluctuation of light intensity through time, and thus, if there are larger particles present in the sample, the measured intensity is much higher than that of smaller NPs. Due to the fact that the light intensity dramatically depends on the particle's size, the presence of even one dust particle can overshadow the NPs in the sample. Thus, the graphical output displaying intensity as a function of the NPs' size can provide misleading information. Displaying either volume or relative frequency number as a function of size is more accurate. In this work, the results from DLS present the relative frequency number as a function of the NPs' size to have a better overview of the hydrodynamic sizes of all particles within our samples (Fig. 5.3).

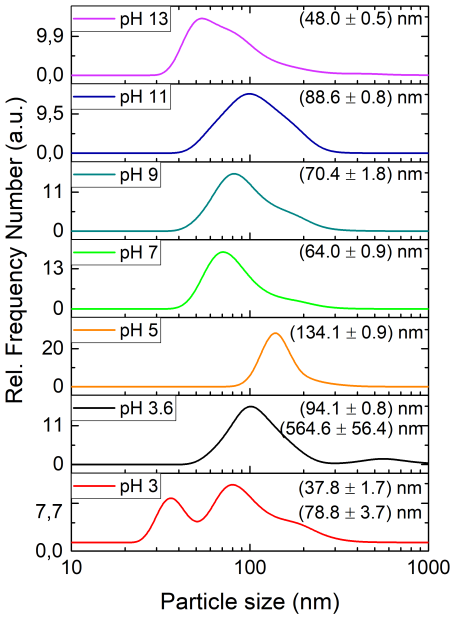

Figure 5.3: DLS size distributions of prepared Pd/FeO_x NPs.

Size distributions obtained from DLS demonstrate much bigger sizes of NPs

compared to those from the TEM analysis. Putting aside the fact that DLS size determination is based on measuring spherical particles, and as observed from TEM our NPs are not purely spherical, such results imply that the measured NPs form larger structures through time, possibly due to their general aggregation or due to the fact that the smaller NPs tend to get attached to the bigger particles' surface; a phenomenon, although long-time ago described as heteroaggregation process, not well understood. As lately described by Alsharif et al. [90], DLVO theory acts as a first approximation to understanding such phenomenon; however, when the system under study is composed of multiple elements, as it is our case, this theory does not provide reliable data. Despite this uncertainty, DLVO theory, accompanied by empirical observations, still allow understanding that the most important factors in heteroaggregation are the colloids' pH conditions, the system's ionic strength, and the components' concentration. Considering our fundamental hypothesis is that pH can modify the element distribution within the produced nanoalloys, pH should be the most crucial factor leading to different heteroaggregation expressions; thus, hydrodynamic size distributions. Aside from modifying ionic strength and elemental composition within the particles, the pH also seems to play a key role in the particles' general aggregation. As observed in Fig.5.3, the samples produced at pH 3 and 13 show the smallest hydrodynamic sizes ($\sim$ 40 nm) out of all samples; in contrast, pH 5 has the largest hydrodynamic size ($\sim$ 134 nm). Considering the classical DLVO theory, a most significant amount of protons within lower pH values (H^+), as well as a larger amount of hydroxide anion (OH^-) within higher pH values, most lead to an increased electrical double layer around the produced NPs [91], thus, an enhanced electrostatic repulsion among particles, resulting in a lower aggregation.

5.1.2 Stability

The trend displayed in Fig. 5.4 shows the decreasing tendency of the ZP from positive to negative values based on the pH of the samples (note that the pH of the solution was approximately the same before and after ablation). This trend is in accordance with the assumption that at a lower pH the positively charged hydrogen ions/protons H^+ are in abundance and, thus, surround the NPs present in the solution leading to a positive ZP value. On the other hand, with higher pH values, the amount of OH^- around the particles increases, leading to negative ZP values. The lower the pH is, the higher the H^+ is, and therefore, the higher the positive ZP values are and vice versa. Note that, since DLS and ZP data heavily depend on the optical values of the particles‘ surface, we measured considering that the particles were purely composed of Fe or Pd. Such an assumption was made to cope with the UV-Vis results suggesting the formation of phase-segregated nanoalloys. Moreover, even when both considerations lead to similar results, TEM images displayed a preferential element distribution of Fe in the nanoalloys shell. Thus, this is the reason why the results displayed herein correspond to nanocolloids considering only Fe optical properties.

The pH at which the ZP is equal to zero, also understood as the pH at which the NP has a net surface charge equal to zero, is the so-called point of zero charge (PZC);

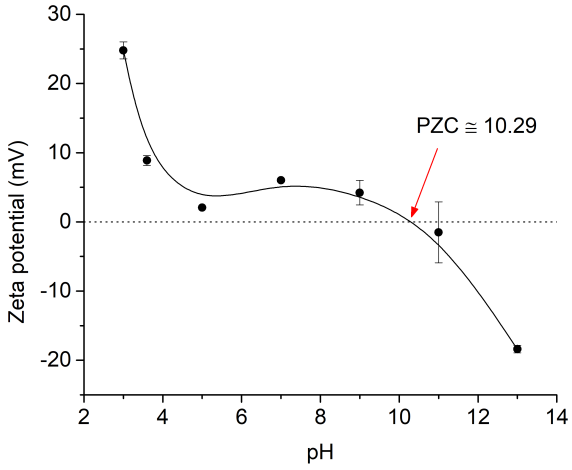

Figure 5.4: Zeta potential of the prepared nanocolloids based on the pH of the Pd salt solution and the point of zero charge (PZC).

in this case, the PZC is around 10.29. Samples exhibiting positive ZP, and accordingly having a pH above the PZC, have a positive surface charge, while samples with negative ZP values have a negative surface charge. The measured ZP values reveal that all samples apart from pH 11 and 13 have a positive surface charge. However, pH 11 also has the most significant standard deviation out of all the samples, and hence, surface charge, in this case, is considered unknown. Samples synthesized at pH 3 and 13 have the highest ZP, 24.8 mV and -18.4 mV, respectively, and thus, are the most stable out of all the samples and are less aggregated. These results follow the hydrodynamic sizes obtained from the DLS measurements, where pH 3 and 13 displayed the smallest size. Although none of the samples exhibited long-term stability, when monitoring them over 3 months, the sample produced at pH 3 was the most stable. The rest of the samples had visible sedimented agglomerates. For further stabilization, it is possible to measure the pH of the clean samples and adjust that accordingly to achieve higher ZP values.

5.1.3 Element distribution

EDX

Firstly, by employing EDX area analysis, we got a general overview of the NPs' composition. The analysis was carried out in the dark field mode, which enables the differentiation of NPs made up of various elements based on the NPs' brightness. In the dark field, NPs composed of heavier atoms are displayed brighter than those composed of lighter atoms. Hence, two areas were selected for the EDX analysis to analyze the different compositions: a brighter and a darker area. From the EDX spectra (Fig. 5.5), it is visible that most of the samples contain both elements (Fe and Pd). However, Fe is the main constituent present in most of the samples and

comprises mainly the outer part of the NPs, while Pd seems to be in a smaller amount covered by Fe. The EDX instrument is a part of TEM, and the signal's intensity is proportional to the concentration of the elements in the sample. Even though TEM has a very high resolution, by employing EDX area analysis, the analyzed area is not actually confined to only the selected area; thus, the resulting spectra of two close areas are then very similar and do not provide the highest detailed information about the sample's composition. Therefore, the EDX analysis gives us only approximate information about the samples' element distribution.

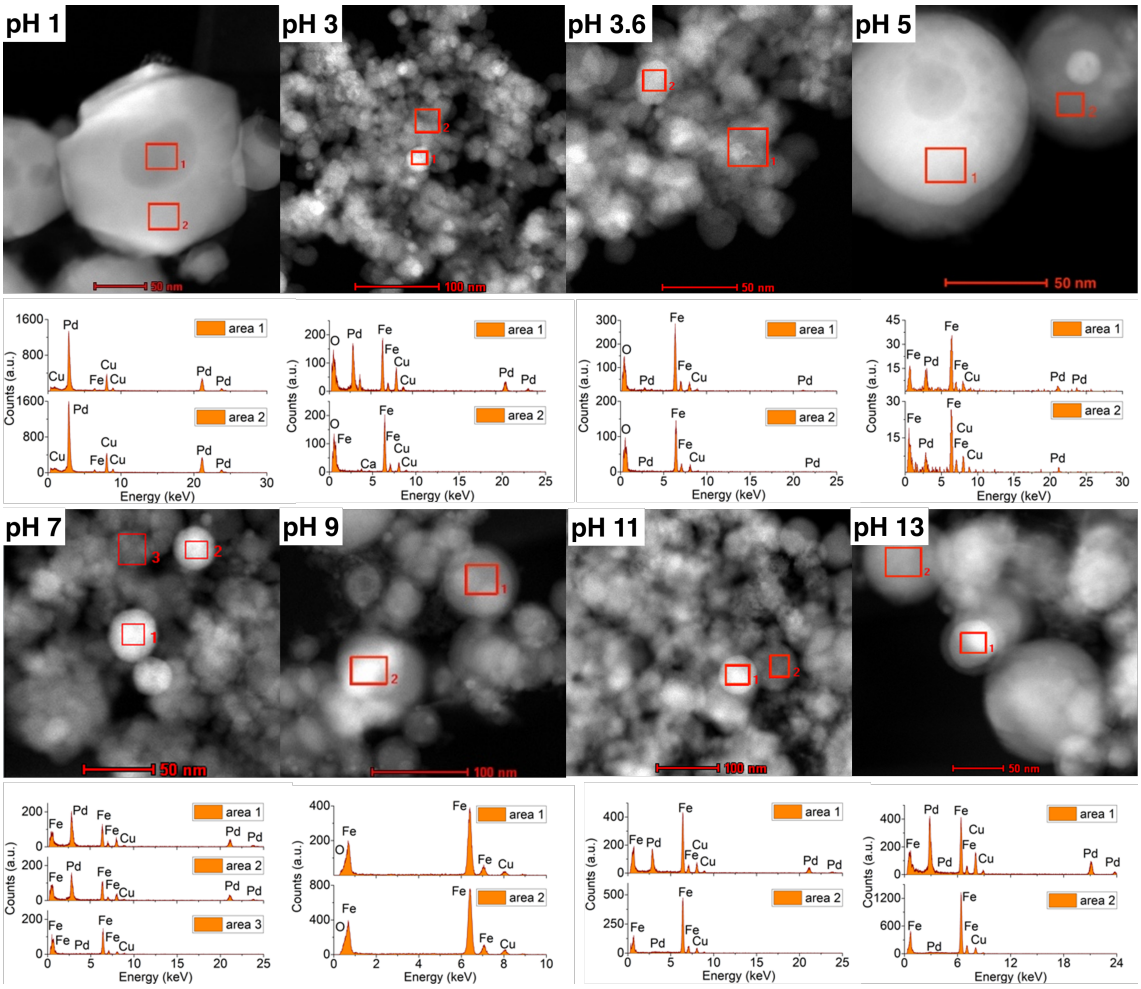

Figure 5.5: EDX area analysis of synthesized Pd/FeO_x NPs.

A deeper inspection indicates that the sample synthesized at pH 1 has the most intense Pd signal out of all the samples and a much lower intensity of Fe signal in both selected areas. On the other hand, EDX spectra of pH 3 reveal two different area compositions. The EDX spectrum of the first (brighter) area shows almost the same Pd and Fe signals intensity, whereas the second (darker) area does not show any peaks belonging to Pd. All EDX spectra contain Cu signals that come from the Cu grid on which the samples are placed. Spectra of pH 3.6 suggest that much lower peak intensities belong to Pd compared to the previous samples' spectra;

however, the Fe signal is stronger in both areas. Samples belonging to pH 3, 3.6, and pH 9 also have visible peaks attributed to oxygen (O). It is thought that most of the samples contain Fe in the form of oxides in the NPs' shell due to oxidation during the synthesis, or it is also likely that O atoms can be adsorbed to the NPs surface during the analysis. However, the O peaks in the EDX spectrum can be overshadowed by Fe peaks, as is the case of pH 9. In pH 5, the two spectra look almost identical; nonetheless, a closer look reveals that the intensity of Pd in the first (brighter) area is slightly higher than that in the second (darker) area. Moreover, in the TEM image of pH 5, a larger Fe-based NP seems to encapsulate the brighter one, which has a much smaller nested Fe-based NP; in addition, the whole structure is covered by many smaller Fe-based NPs, which is why we observe more intense Fe signal than the one attributed to Pd. Even though the NP is similar to the one in pH 1, it is twice as small, and thus, the signals differ. For pH 7, there were three areas selected: two brighter areas and one darker area. The spectra of the brighter areas have a more intense Pd signal, whereas the spectrum of the darker area has barely any Pd signal. However, the Fe peaks have a consistent intensity in all three spectra. The spectra of pH 9 stand out from the rest of the samples because none of the spectra contain peaks belonging to Pd. After a thorough analysis of the TEM image, it is possible to conclude that the brighter area is not only indicative of a heavier element. Rather, it can indicate the result of the NPs (most likely Fe/FeO_x) stacking or Fe encapsulation of extremely small nested Pd NPs. Although EDX analysis did not provide information on Pd content in the sample synthesized at pH 9, possibly due to the overshadowing of Fe signal, alternative and more precise methodologies must be considered to complement the current findings. The spectra of pH 11 are contrasting; the brighter area has more Pd content than the darker area from which the spectrum obtained contains a very small Pd peak, though the intensity of the Fe signals stays stable. Lastly, pH 13 seems to have intense Pd and Fe signals coming from the first area; however, in the spectrum of the second area, the Pd peak almost disappears, leaving only peaks attributed to Fe, similarly to the first spectrum. Overall, EDX spectra correlate well with the element distribution assumptions made in the previous subchapters, i.e., mostly phase-segregated alloys are created where, except for pH 1, Pd is encapsulated by Fe, either in the form of a shell or in the form of small NPs.

HR-TEM

To gain more detailed information about the NPs' element distribution, HR-TEM analysis was employed. In HR-TEM images, the individual atoms (electron shells) are visible, allowing the space measurements between the atomic planes in a crystal lattice (d-spacing). The measurements were carried out using ImageJ, and the crystallographic families were assigned to the measured d-spacings according to the databases of the international centre for diffraction data (ICDD). The results from the HR-TEM analysis are seen in Fig. 5.6. In addition, all data corresponding to the analysis can be found in Tab.A.1 in the Appendix. Due to the very precise analysis of different parts of a single NP, this method gave a much more detailed

analysis of the prepared NPs than EDX. For instance, the samples' darker sides always lead to the identification of the tetragonal FePd crystal (ICDD file: 2-1440), whereas the brighter sides lead to the identification of the rhombohedral FeO crystal (ICDD file: 6-711), or as displayed in pH 3.6 and pH 5, also to the face-centered cubic Fe_3O_4 crystal (ICDD file: 26-1136). The only sample that does not follow such tendency is pH 5, in which, although dark parts were selected for analysis, no crystalline families belonging to Pd were found. Considering HR-TEM is performed in bright field mode, the brighter areas within the particles also imply a larger number of electrons being transmitted through and, thus, a clearer overview of atomic arrangement within the studied crystalline particles. Since the selected dark area in pH 5 consisted of a small particle nested in a bigger and brighter one, we believe the crystalline structure belonging to Pd could be overshadowed by those of the brighter element belonging to the two identified forms of Fe oxide. The same effect led to a completely different observation phenomenon when analyzing the brighter small particles nested in big dark particles in pH 1, resulting in the clear identification of nested Fe oxide small particles within FePd big NPs.

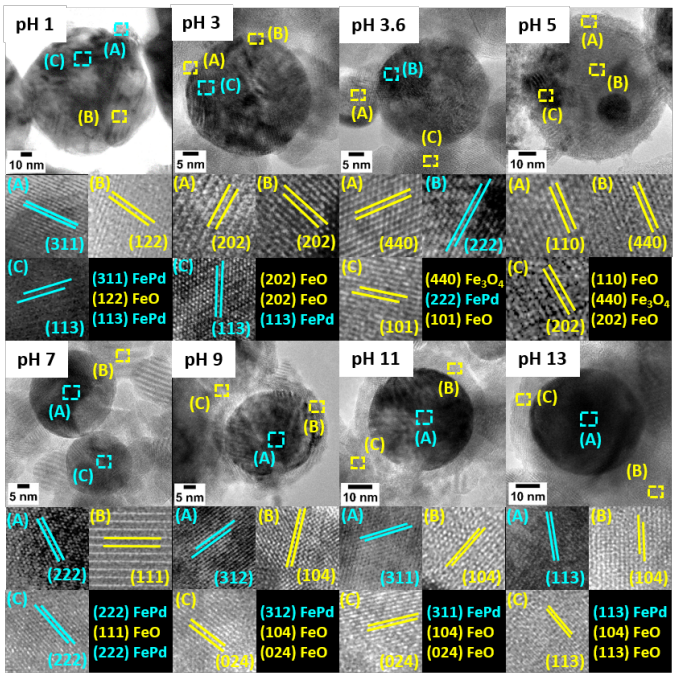

Figure 5.6: HR-TEM analysis of synthesized Pd/FeO_x NPs.

An additional piece of information worth highlighting is that in most cases, it was possible to identify high-index facets, denoted by a set of Miller indices $\{hkl\}$ where at least one of them is greater than the unity. This is typical when employing out-of-equilibrium conditions for the synthesis of nanomaterials, which is the case of RLAL [92]. Such anomalous crystallographic structures permit, among others, to form materials that partially contradict the Hume-Rothery theory; for instance, although phase-segregated, FePd facets within the particles. Moreover, aside from creating geometries favoring the formation of MSI sites, these so-called high-index

facets have a high density of low-coordinated atoms, such as kinks, steps, or edges that serve as additional active catalytic sites [93].

SAED

SAED, which is an even more precise analysis, was employed to expand the information about our NPs element distribution. The HAADF images obtained were analyzed using ImageJ, and the d-spacing was calculated from the measured 1/2r values (r is the wanted d-spacing). Finally, the obtained d-spacing was matched with the ICDD databases to identify the crystal systems correctly. All data corresponding to the analysis can be found in Tab.A.2 in the Appendix.

In Fig. 5.7 the SADPs are made up of concentric rings meaning the samples mainly consist of poly-crystalline NPs. Moreover, SAED revealed some new crystal systems not previously identified using HR-TEM. Apart from the Fe oxides and FePd crystals that were already detected, most samples seem to have pure cubic Fe crystals (ICDD files: 52-513, 85-1410). In addition, pure cubic Pd crystals (ICDD file: 65-2867) were identified in samples pH 1 and 13. These results coincide with EDX analysis, where the highest Pd signals were found in spectra of pH 1 and 13. Moreover, in pH 5, FePd and PdO_2 crystals were readily found, which were not identified in HR-TEM analysis. However, Pd peaks were visible in the EDX spectra of pH 5; thus, SAED analysis confirmed that Pd is present in the form of an alloy and an oxide.

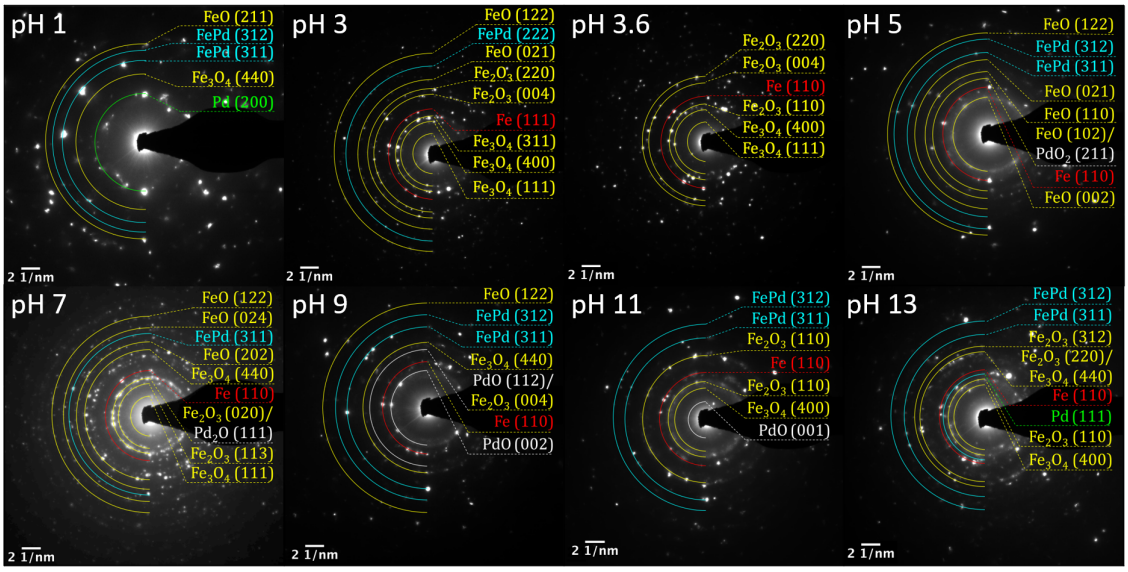

Figure 5.7: SAED analysis of synthesized Pd/FeO_x NPs. SAED patterns of all the samples with assigned Miller indices differentiated by colours based on the associated crystals.

Although EDX analysis did not provide information on O peaks in all the samples, the SAED analysis confirmed that all samples contain Fe in the form of oxides. The most commonly found Fe oxide crystals are rhombohedral FeO (ICDD file:

6-711), cubic Fe_3O_4 (ICDD file: 79-416, 74-748), orthorhombic Fe_3O_4 (ICDD file: 76-955), hexagonal Fe_2O_3 (ICDD file: 40-1139), orthorhombic Fe_2O_3 (ICDD file: 47-1409) and rhombohedral Fe_2O_3 (ICDD file: 79-7). Even though Pd oxides are rarely assigned, the few times they are, they have different Pd:O content ratios, crystal systems, and Miller indices. For example, in pH 5, tetragonal PdO_2 crystal with Miller index (211) (ICDD file: 34-1101) can be found; however, in pH 7, cubic Pd_2O crystal with Miller index (111) (ICDD file: 65-5065) is found. Moreover, in the SADP of pH 9, two tetragonal PdO crystals with different Miller indices are identified (ICDD files: 85-624, 75-200), and lastly, in pH 11 d-spacing attributed to tetragonal PdO crystal with Miller index (002) (ICDD files: 75-200) is assigned. The only sample that does not have any Pd or Pd-based crystals identified is pH 3.6, despite having Pd signals in EDX analysis and assigned FePd crystals in HR-TEM analysis. The reason for such inaccuracy is related to the impossibility of observing diffraction points following larger-sized ring patterns, a phenomenon often related to the selection of regions with a large number of agglomerated NPs, which can be a side effect of NPs aggregation before the samples' preparation for TEM-related analyses. An additional side effect of this is that two crystals are assigned in some cases because the d-spacings belonging to the ring patterns are not differentiated enough to select the proper crystal precisely. For instance, in the SADP of pH 5 a hexagonal FeO crystal (102) with 1.686 Å d-spacing and tetragonal PdO_2 (211) crystal with 1.681 Å d-spacing are assigned. As in the case of HR-TEM analysis, this analysis also allowed the identification of high-index facets, which, as stated before, is typical for RLAL. Overall, by employing SAED analysis, we were able to confirm the results of the HR-TEM analysis and assign new crystal systems that gave us a deeper insight into the element distribution of all the samples.

ICP-OES

Lastly, ICP-OES allowed a more general quantitative overview of the samples' composition. As displayed in Tab.5.1, all samples display a > 87 % Fe and < 13 % Pd composition. This result greatly correlates with the initially employed Pd salt concentration of 0.1 mM, which can lead to a maximum Pd concentration of 56.94 mg/L within the samples. Note that the current calculation was done considering that after samples' cleaning, their solid content was collected in single 1.5 mL Eppendorfs, which were further employed for the ICP-OES measurements.

The ICP-OES data also shows that the pH variation influences the total amount of Pd composing the NPs. Although the composition varies slightly, we can infer that the origin of such modification lies in the interplay between the ionic spices employed to control the pH of the samples and the K_2PdCl_4. As discussed in Chapter 1, during the RLAL process, a portion of the total metal salt amount can be transferred into the ablation plasma, forming, in this way, part of the new NPs. However, the amount that was not transferred into the plasma can be further reduced over the recently created NPs surface. Since $PdCl_4^{2-}$ are the Pd spices interfering in the alloy formation, they would need to compete for a space at the NPs surface with the ions used to modify the pH, i.e., H^+ and Cl^- in case of HCL,

and K^+ and OH^- for KOH. Such chaotic interplay between various amounts of different charges can result in variation within the final NPs composition. Thus, we can conclude from this observation that, although the hypothesis of pH modification leading to the control of NPs element distribution is very appealing, it necessary to keep in mind that it can also affect their element composition. Moreover, given the out-of-equilibrium conditions leading to a chaotic interplay between species at the NPs surface, the final NPs atomic composition can be only estimated in terms of the amount of used metal salt but not precisely predicted.

Sample	**Fe (mg/L)**	**Pd (mg/L)**	**Fe (at.%)**	**Pd (at.%)**
pH 1	0.011030	0.003131	87.03	12.97
pH 3	357	47.3	93.49	6.51
pH 3.6	169	43.7	88.05	11.95
pH 5	154	33.3	89.81	10.19
pH 7	500	45.2	95.46	4.54
pH 9	179	48.8	87.47	12.53
pH 11	206	50.7	88.57	11.43
pH 13	211	42.4	90.46	9.54

Table 5.1: Atomic percentages of Fe and Pd in all the samples from ICP-OES.

5.2 Magnetic properties

The magnetic properties of the synthesized Pd/FeO_x NPs are essential because the material we are aiming for would find application in catalysis. Thus, having a catalyst with significant magnetic properties would allow it to be efficiently recycled. In this work, Fe foil was used for the synthesis, and from the previous analysis we know that the NPs contain Fe in the form of oxides (FeO, Fe_2O_3, Fe_3O_4) as well as alloy (FePd). Hence, we predict that the NPs should be easily manipulated when exposed to an external magnetic field. In order to know the magnitude of magnetization, the NPs underwent VSM analysis.

The results obtained from VSM measurements are displayed in Fig. 5.8. The magnetization curves visible are the so-called hysteresis loops which are typical for ferromagnetic materials. The exact values of saturation (M_s), remanence (M_r), coercivity (H_C), as well as the remanent ratio (R)= M_r/M_S and anisotropy constant (K) of the samples are summarized in Tab. 5.2. There is a noticeable trend where there is an increase in magnetization values with an increasing pH of the sample, more precisely, an increase in M_s values. The only sample not adhering to this trend is pH 3, which has a higher M_s value than pH 3.6 and 5. Otherwise, the trend applies to all the samples. The highest M_s value is reached at pH 13 (183.333 emu·g^{-1}), on the other hand, the lowest M_s values belongs to pH 3.6 (64.041 emu·g^{-1}). The highest M_s value measured is close to that of pure iron (221.71 ± 0.08 emu/g) [94].The magnetization depends in this case on many different factors: the Fe:Pd content ratio, or the oxidation states of iron, for instance, Fe_3O_4 is ferrimagnetic [95],

Fe_2O_3 exhibits weak ferromagnetism at room temperature and antiferromagnetism below 260 K [96], and FeO is paramagnetic at room temperature [97]. Moreover, it also depends on the NPs size [98] and their structure, i.e., the magnetic behavior would vary if the particles are phase-segregated [99]. Thus, to correctly interpret the results of the VSM measurements, it is necessary to consider all of these factors.

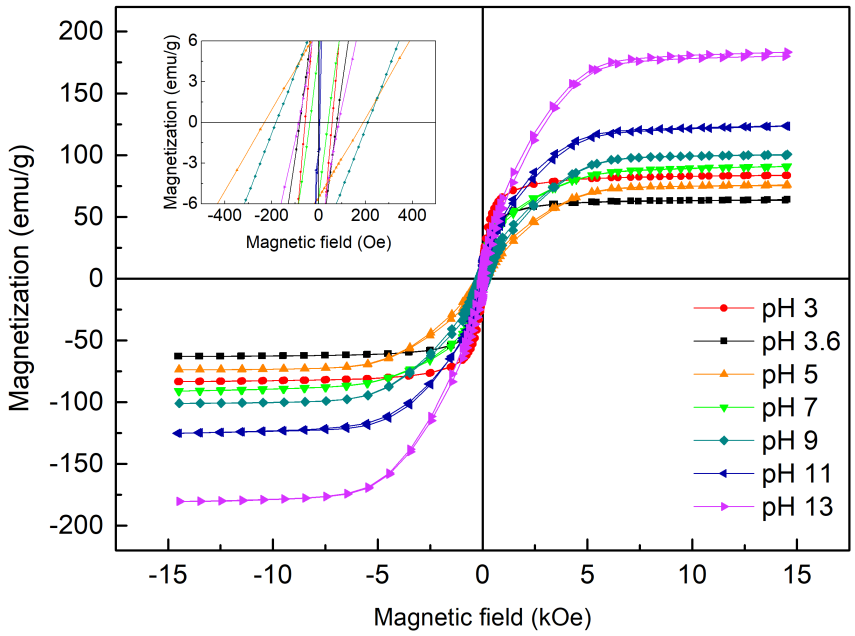

Figure 5.8: Hysteresis loop of all samples subjected to magnetization by an external magnetic field in VSM measurement.

As observed in Tab. 5.2, the principal factor influencing the samples‘ magnetic behavior seems to be the pH variation when creating the NPs. This correlates well with the UV-Vis and TEM data, where the encapsulation of Fe reduces with increasing pH, leading to a preferential formation of Pd@Fe. As suggested by Aguilera-del-Toro et al. [99], this implies that the quenched spin polarization of the Fe species by the non-magnetic element Pd would decrease when increasing pH, resulting in larger magnetization values as the pH increases. Moreover, pH 13 has the highest M_s value which can be due to the bigger size of the NPs [100], as observed in TEM size measurements. The amount of Pd, in addition, can explain the decrease in magnetization; the more the Pd there is, the worse the magnetization of the sample is. From ICP-OES, it is known that pH 3 has a lower at.% of Pd than pH 3.6 and 5, thus explaining the anomaly in the trend of increased M_s with higher pH.

Finally, a negative M_r value was measured for pH 11 accompanied by an extremely low H_C, which applications prospects are still under study [101]. Although this is a very unusual and still controversial phenomenon, there are some examples in the literature reporting this effect in core-shell nanoalloys or nanostructures with

Sample	M_S (emu·g^{-1})	M_r (emu·g^{-1})	H_C (Oe)	M_r/M_S (a.u.)	K (emu·Oe·g^{-1})
pH 3	83.681	11.370	58	0.136	4951
pH 3.6	64.041	10.200	80	0.159	5226
pH 5	75.977	6.926	231	0.091	17902
pH 7	90.988	5.311	37	0.058	3434
pH 9	100.630	8.036	181	0.080	18578
pH 11	123.271	-1.970	2	-0.016	189
pH 13	183.333	10.729	85	0.059	15895

Table 5.2: Measured saturation (M_s), remanence (M_r), coercivity (H_C) and calculated remanent ratio (R)= M_r/M_S and anisotropy constant (K) of the samples from VSM analysis.

segregated phases in the core-shell form [102, 103, 104]. As described by Gu et al. [101], this phenomenon is a consequence of the interplay between the core and shell spins within core-shell NPs. When the applied field is sufficiently large, core and shell spins can align to the applied field. However, when the field is reduced, as it occurs in VSM, the superficial or shell spins can fluctuate. In contrast, the core spins remind frozen, leading to an antiparallel spin alignment between core and shell spins resulting in negative remanent magnetization. Even though this is an improbable phenomenon to happen at room temperature, and possibly the reason why we do not observe it in most cases, some phase-segregated nanomaterials can display it, as is the case of NPs synthesized at pH 11.

5.3 MSI determination

The SMSI/MSI effect was assessed through the measurement of the synthesized NPs catalytic activity. For this, we employed the model reduction of the 4-NP pollutant, as described in Chapter 3. By measuring the absorbance at 401 nm, we created the graphs seen in Fig. 5.9 A. These graphs show that the absorbance is both time- and concentration-dependent. Thus, the longer the reaction time is, the lower the absorbance is. As a result, the reduction of 4-NP is visible in all the graphs, apart from the lowest concentration (top left graph Fig. 5.9A), which displays only a slightly decreasing tendency. However, as can be seen in the graph corresponding to the highest concentration employed (bottom right Fig. 5.9A), the absorbance rapidly decreases at first, but at some point, it starts to slowly increase again, which is attributed to the excess amount of catalyst present after the reaction took place. In general, a higher catalyst concentration (catalyst dose) leads to a higher reaction rate which can be seen in the more rapid decrease of the absorbance. This occurs due to the increased amount of NPs in the reactor, hence, the increased number of active sites that enable electron transfer.

The reaction rate constant as a function of the catalyst dose is presented in Fig. 5.9 B for all the samples. From these results, we observe that the highest catalytic

activity, and thus, the highest kinetic rate constant (k_{app}) belongs to pH 9 with an activity parameter (κ_c) of (2.03 ± 0.08) L/g·s. This sample has a high k_{app} (0.001 s^{-1}) even for the lowest catalyst dose (1.48 mg/L). On the contrary, pH 13 displays the worst catalytic activity, having a κ_c of (0.64 ± 0.08 L/g·s). The rest of the samples seem to have quite a similar tendency. Samples synthesized at pH 3 and 3.6, in particular, have almost identical κ_c values (1.27 ± 0.13 L/g·s) and (1.22 ± 0.23) L/g·s, respectively. Moreover, pH 5 also posses high κ_c (1.64 ± 0.16) L/g·s.

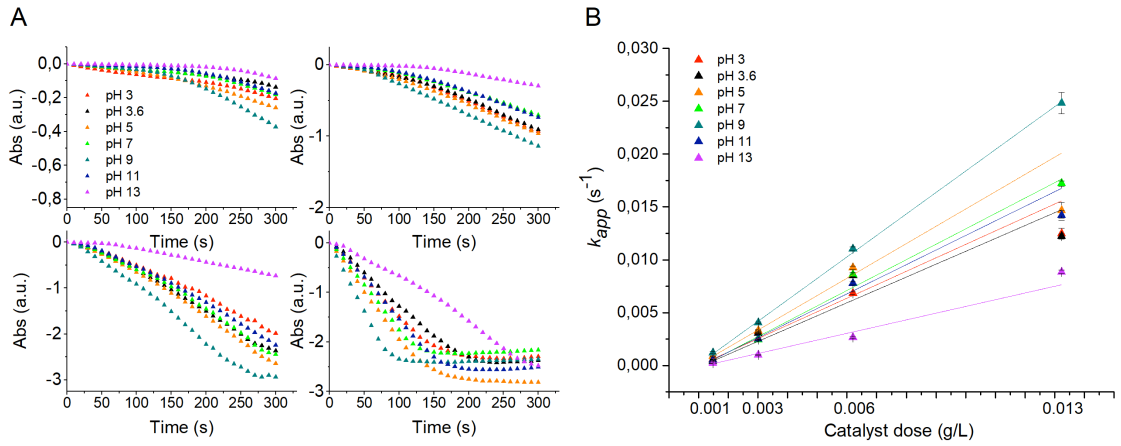

Figure 5.9: Results of UV-Vis monitoring of 4-NP degradation at 401 nm for 4 different concentrations of NPs (A) and the change of the obtained kinetic rate constant based on the catalyst dose (B). Note that the sample synthesized at pH 1 could not be tested due to the small amount produced.

The reaction diagram (Fig. 5.10) illustrating the NP-mediated hydrogenation of 4-NP, shows that such six electron-powered transformations from 4-NP to 4-AP heavily depend on the electron transfer from the NPs. For the electron transfer to occur, both the $[BH_4]^-$ and 4-nitrophenolate anions must be adsorbed to the NPs surface. Thus, a crucial factor influencing the catalysis is the surface charge of the NPs, which affects the ability of the reactants to adsorb to the NPs' surface. Namely, in the case of 4-NP reduction, positively charged NPs should have enhanced catalytic activity because 4-NP dissociates to the 4-nitrophenolate anion. Thus, the negatively charged ions can easily attach to the positively charged NPs. In our case, the ZP measurements reveal that most of the NPs, except those belonging to pH 13 and possibly pH 11, have a positively charged surface. Hence, it is expected that the negatively charged species would be attracted to the NPs possessing the highest positive ZP value; this indicates that pH 3 should exhibit the best catalytic activity. However, the screening tests revealed that pH 9 serves as the best catalyst for 4-NP reduction, so it is necessary to consider other factors contributing to the overall catalytic activity.

As it is well known, the catalytic activity increases with decreasing size of the particles due to the higher surface area, ultimately leading to an increased number of active sites [105]. From the TEM size measurements and DLS hydrodynamic size assessment, we know that samples synthesized at pH 3, 5, 7, 9, and 13 contain

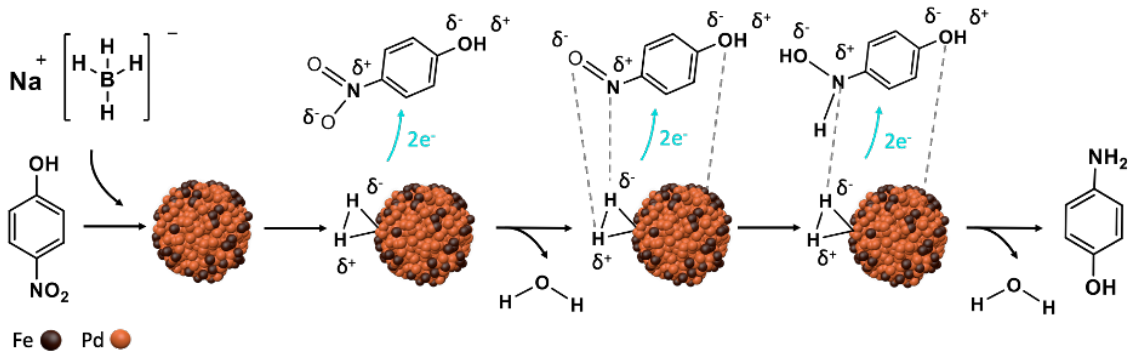

Figure 5.10: Reaction mechanism of 4-NP degradation catalysed by Pd/FeO_x NPs.

the highest amount of small NPs. In addition, ICP-OES revealed that the samples containing the highest at.% of the catalytically active element, i.e., Pd, are those synthesized at pH 1, 3.6, 9, and 11. Thus, although the differences are minimal, the sample combining all these aspects is pH 9; therefore, it is expected that such sample displays the best catalytic activity. However, considering the most significant effect leading to an efficient catalytic activity during the performed model reaction is the materials surface charge, the above reasoning still does not fully explain why the sample synthesized at pH 9 displays an almost 2-fold κ_c increment when compared to the sample synthesized at pH 3.6 ((2.03 $\pm$ 0.08) L/g·s and (1.21 $\pm$ 0.23) L/g·s, respectively). Although the sample pH 3.6 shows a slight size difference compared with pH 9, it still presents the largest positive superficial charge associated with a ZP value of (8.87 $\pm$ 0.73) mV. Thus, the fact that their catalytic activity is not comparable points out an additional phenomenon.

To the best of our knowledge, two additional phenomena result in catalytic response increment, high-index facet formation, and SMSI/MSI effect. Since all samples present high-index facet formation, the remaining option for such catalytic activity difference lies in the SMSI/MSI effect. As discussed in Chapter 1, SMSI occurs when a noble metal is encapsulated by an oxide support (usually a reducible oxide), yet there are still spaces where the interface between both elements interacts with the molecules involved in the catalytic reaction [62]. In our case, Pd can act as the encapsulated noble metal and the Fe oxide species as the oxide support. Since our morphology and element distribution results display the required conditions for SMSI site formation, it is plausible to consider that such an effect is leading to the outstanding catalytic behavior of the sample synthesized at pH 9. Thus, we conclude that the pH modification when synthesizing Pd-Fe nanoalloys by RLAL can result in such a manipulation over the NPs element distribution that the formation of SMSI sites is promoted. Moreover, considering these structures displaying the SMSI effect also exhibit a relatively high saturation magnetization value, they can serve as optimal reusable catalysts.

6 Conclusion

The current thesis explores the implication of modifying the pH conditions when synthesizing NPs composed of Pd and Fe by RLAL. Our proposition is that pH modification can influence the nucleation mechanism in the formed NPs to the point that by controlling the pH, we can manipulate the element distribution within the synthesized NPs. This is a powerful concept that can result in the formation of either metal support interactions (MSI) or strong metal support interactions (SMSI) between the noble metal "Pd" and the metal oxide "FeO_x" depending on the elements' disposition within the produced materials. Since these effects are considered some of the few tools able to enhance the catalytic performance of heterogeneous catalysts, it is envisaged that the element distribution manipulation resulting in SMSI or MSI would bring outstanding benefits to the catalysis field.

Our results indicate that although the system Pd-Fe can hardly form substitutional alloys, the RLAL synthesis approach can force the formation of phase-segregated nanoalloys encompassing structures like nested and core-shell NPs, and big NPs decorated by smaller ones. Moreover, the liquid medium pH modification influences the final nanoalloys element distribution, where pH < 3 leads to Fe small particles encapsulation by bigger Pd NPs (37.6 ± 4.0 nm), also referred to as nested NPs. Whereas, for pH > 3, Fe tends to form the shell of Pd@Fe NPs, encapsulate Pd in the form of nested small NPs, or decorate the surface of bigger particles in the form of small NPs (sizes of found particles from (6.1 ± 0.5) nm to (51.4 ± 1.0) nm). Together with the observed element distribution, these types of structures can result in SMSI or MSI effects. The crystalline analysis of these segregated phases, in addition, indicates that Fe is present in most of the samples as pure Fe or in the form of different types of oxides like FeO, Fe_2O_3, and Fe_3O_4. On the other hand, Pd can be found as PdFe in all the particles and as pure Pd when using pH 1 and 13. Moreover, all the samples show high-index facets (Miller indices where at list one is greater than the unity), implying that the kinks, steps, or edges immanent to them can contribute to the particles' overall catalytic activity by offering low-coordinated atom sites.

The NPs element distribution also strongly influences their magnetic properties, leading to an enhanced magnetic response with an increased amount of Fe on their surface, thus, resulting in better structures for catalyst recyclability. Moreover, as exhibited by the sample synthesized at pH 11, this type of element distribution found in segregated phases can result in negative remanent magnetization that, even though it is a very unusual and still controversial phenomenon, can find interesting applications in the future. Finally, the catalytic activity screening assessed through

the efficiency in the model 4-NP reduction shows that the overall NPs structure also leads to the expression of the SMSI effect. In particular, the sample synthesized at pH 9 displays the most significant catalytic activity, which is attributed to the formation of SMSI sites, explaining why, even when its element composition/distribution or superficial charge (corresponding to a ZP = 4.22 ± 1.78 mV) are not optimal, it still yields the best catalytic performance (κ_c = 2.03 ± 0.08 L/g·s).

Overall, the current results prove that the pH modification when employing RLAL can result in the element distribution manipulation within phase-segregated nanoalloys. This results in nanoalloy physicochemical properties tuning, like their magnetic response manipulation or their catalytic activity enhancement through the appearance of high-index facets and the SMSI effect. As amply discussed by the scientific community interested in the design of efficient catalysts, this striking finding able to exert an improvement in the catalytic response in nanoalloys formed by immiscible elements can be of fundamental importance for the future development of truly tailored designed catalysts. Moreover, the element distribution control over magnetic nanoalloys not only carries benefits to the field explored in the current thesis, but it is also expected that the reaction rates, and equilibria, among other results obtained experimentally herein, can be further used in theoretical science. In particular, for predicting chemical reaction pathways/rates powered by multielement nanomaterials.

References

[1] FEYNMAN, Richard P. There's plenty of room at the bottom. *Engineering and science*. 1959, vol. 23, no. 5.

[2] TALEBIAN, Sepehr; RODRIGUES, Tiago; NEVES, José das; SARMENTO, Bruno; LANGER, Robert; CONDE, João. Facts and Figures on Materials Science and Nanotechnology Progress and Investment. *ACS Nano*. 2021, vol. 15, no. 10, pp. 15940–15952. ISSN 1936-0851, 1936-086X. ISSN 1936-0851, 1936-086X. Available from DOI: 10.1021/acsnano.1c03992.

[3] GUO, Chunlei; SINGH, Subhash Chandra. *Handbook of Laser Technology and Applications: Lasers Applications: Materials Processing and Spectroscopy (Volume Three)*. CRC Press, 2021.

[4] GUO, Chunlei; SINGH, Chandra Subhash. *Handbook of Laser Technology and Applications: Laser Applications: Medical, Metrology and Communication (Volume Four)*. CRC Press, 2021.

[5] FOJTIK, Anton; HENGLEIN, Arnim. Laser ablation of films and suspended particles in a solvent: formation of cluster and colloid solutions. *BERICHTE-BUNSENGESELLSCHAFT FUR PHYSIKALISCHE CHEMIE*. 1993, vol. 97, pp. 252–252.

[6] JOHN, Mallory G.; TIBBETTS, Katharine Moore. Controlling the morphology of copper-silica nanocomposites from laser ablation in liquid. *Applied Surface Science*. 2020, vol. 510, pp. 145037. ISSN 01694332. Available from DOI: 10.1016/j.apsusc.2019.145037.

[7] ETTEL, David et al. Laser-synthesized Ag/TiO nanoparticles to integrate catalytic pollutant degradation and antifouling enhancement in nanofibrous membranes for oil–water separation. *Applied Surface Science*. 2021, vol. 564, pp. 150471.

[8] LIU, Jixing et al. Deep understanding of strong metal interface confinement: a journey of Pd/FeO x catalysts. *ACS Catalysis*. 2020, vol. 10, no. 15, pp. 8950–8959.

[9] KOSAKA, P. M.; PINI, V.; RUZ, J. J.; SILVA, R. A. da; GONZÁLEZ, M. U.; RAMOS, D.; CALLEJA, M.; TAMAYO, J. Detection of cancer biomarkers in serum using a hybrid mechanical and optoplasmonic nanosensor. *Nature Nanotechnology*. 2014, vol. 9, no. 12, pp. 1047–1053. Available from DOI: 10.1038/nnano.2014.250.

[10] YAN, Yong; WARREN, Scott C.; FULLER, Patrick; GRZYBOWSKI, Bartosz A. Chemoelectronic circuits based on metal nanoparticles. *Nature Nanotechnology*. 2016, vol. 11, no. 7, pp. 603–608. Available from DOI: 10.1038/nnano.2016.39.

[11] ZIJLSTRA, Peter; PAULO, Pedro M. R.; ORRIT, Michel. Optical detection of single non-absorbing molecules using the surface plasmon resonance of a gold nanorod. *Nature Nanotechnology*. 2012, vol. 7, no. 6, pp. 379–382. Available from DOI: 10.1038/nnano.2012.51.

[12] CHEN, Shihong; YUAN, Ruo; CHAI, Yaqin; HU, Fangxin. Electrochemical sensing of hydrogen peroxide using metal nanoparticles: a review. *Microchimica Acta*. 2013, vol. 180, no. 1, pp. 15–32.

[13] ACHARYA, Rituparna. *A Comprehensive Guide to Nanoparticles in Medicine*. Bentham Science Publishers, 2021.

[14] ZHANG, Lijie Grace; LEONG, Kam; FISHER, John P. *3D bioprinting and nanotechnology in tissue engineering and regenerative medicine*. academic press, 2022.

[15] ALEXANDRESCU, Vlad. *Wound Healing: New insights into Ancient Challenges*. BoD–Books on Demand, 2016.

[16] KORKIN, Anatoli; GUSEV, Evgeni; LABANOWSKI, Jan K; LURYI, Serge. *Nanotechnology for electronic materials and devices*. Springer Science & Business Media, 2010.

[17] PHILIPPOT, Karine; ROUCOUX, Alain. *Nanoparticles in Catalysis: Advances in Synthesis and Applications*. John Wiley & Sons, 2021.

[18] EL-ESKANDARANY, M Sherif; AL-HAZZA, Abdulsalam; AL-HAJJI, Latifa A; ALI, Naser; AL-DUWEESH, Ahmed A; BANYAN, Mohammad; AL-AJMI, Fahad. Mechanical milling: a superior nanotechnological tool for fabrication of nanocrystalline and nanocomposite materials. *Nanomaterials*. 2021, vol. 11, no. 10, pp. 2484.

[19] SUGIOKA, Koji; CHENG, Ya. *Laser-Based Nano Fabrication and Nano Lithography*. MDPI, 2018.

[20] HUANG, Zhipeng; GEYER, Nadine; WERNER, Peter; DE BOOR, Johannes; GÖSELE, Ulrich. Metal-assisted chemical etching of silicon: a review: in memory of Prof. Ulrich Gösele. *Advanced materials*. 2011, vol. 23, no. 2, pp. 285–308.

[21] YAN, Juanzhu; TEO, Boon K; ZHENG, Nanfeng. Surface chemistry of atomically precise coinage–metal nanoclusters: from structural control to surface reactivity and catalysis. *Accounts of Chemical Research*. 2018, vol. 51, no. 12, pp. 3084–3093.

[22] KHARISOV, Boris I; KHARISSOVA, Oxana V. Handbook of Greener Synthesis of Nanomaterials and Compounds: Volume 1: Fundamental Principles and Methods. 2021.

[23] ABID, Namra et al. Synthesis of nanomaterials using various top-down and bottom-up approaches, influencing factors, advantages, and disadvantages: A review. *Advances in Colloid and Interface Science*. 2021, pp. 102597.

[24] COVIELLO, Vito; FORRER, Daniel; AMENDOLA, Vincenzo. Recent developments in plasmonic alloy nanoparticles: synthesis, modelling, properties and applications. *ChemPhysChem*. 2022. Available from DOI: 10.1002/cphc.202200136.

[25] KARIMI-MALEH, Hassan; CELLAT, Kemal; ARIKAN, Kubilay; SAVK, Aysun; KARIMI, Fatemeh; ŞEN, Fatih. Palladium–Nickel nanoparticles decorated on Functionalized-MWCNT for high precision non-enzymatic glucose sensing. *Materials Chemistry and Physics*. 2020, vol. 250, pp. 123042. Available from DOI: 10.1016/j.matchemphys.2020.123042.

[26] CHATURVEDI, Shalini; DAVE, Pragnesh N; SHAH, NK. Applications of nano-catalyst in new era. *Journal of Saudi Chemical Society*. 2012, vol. 16, no. 3, pp. 307–325.

[27] JOHNY, Jacob et al. Multidimensional thermally-induced transformation of nest-structured complex Au-Fe nanoalloys towards equilibrium. *Nano Research*. 2021, vol. 15, no. 1, pp. 581–592. Available from DOI: 10.1007/s12274-021-3524-7.

[28] FERRANDO, Riccardo; JELLINEK, Julius; JOHNSTON, Roy L. Nanoalloys: From Theory to Applications of Alloy Clusters and Nanoparticles. *Chemical Reviews*. 2008, vol. 108, no. 3, pp. 845–910. Available from DOI: 10.1021/cr040090g.

[29] LI, Yangyang; ZHANG, Yunshang; QIAN, Kun; HUANG, Weixin. Metal–Support Interactions in Metal/Oxide Catalysts and Oxide–Metal Interactions in Oxide/Metal Inverse Catalysts. *ACS Catalysis*. 2022, vol. 12, no. 2, pp. 1268–1287. Available from DOI: 10.1021/acscatal.1c04854.

[30] WANG, Qingqing; WANG, Jinling; JIANG, Shengxiang; LI, Pingyun. Recent Progress in Sol-Gel Method for Designing and Preparing Metallic and Alloy Nanocrystals. *Acta Physico-Chimica Sinica*. 2019, vol. 35, no. 11, pp. 1186–1206. Available from DOI: 10.3866/pku.whxb201902002.

[31] LI, Si-jia; PING, Yun; YAN, Jun-Min; WANG, Hong-Li; WU, Ming; JIANG, Qing. Facile synthesis of AgAuPd/graphene with high performance for hydrogen generation from formic acid. *Journal of Materials Chemistry A*. 2015, vol. 3, no. 28, pp. 14535–14538. Available from DOI: 10.1039/c5ta03111g.

[32] LIU, Zhaolin; ZHANG, Xinhui. Carbon-supported PdSn nanoparticles as catalysts for formic acid oxidation. *Electrochemistry Communications*. 2009, vol. 11, no. 8, pp. 1667–1670. Available from DOI: 10.1016/j.elecom.2009.06.023.

[33] PEIXOTO, E.B.; CARVALHO, M.H.; DUQUE, J.G.S.; MURACA, D.; XING, Y.T.; NUNES, W.C. Size distribution and interaction effects on dispersed Fe30Ni70 nanoalloy synthesized by thermal decomposition. *Journal of Magnetism and Magnetic Materials*. 2021, vol. 518, pp. 167399. Available from DOI: 10.1016/j.jmmm.2020.167399.

[34] WAN, Jinxin; LIU, Zhenyuan; YANG, Xiaoyu; CHENG, Peng; YAN, Chao. Cyanogel-Derived Synthesis of Porous PdFe Nanohydrangeas as Electrocatalysts for Oxygen Reduction Reaction. *Nanomaterials*. 2021, vol. 11, no. 12, pp. 3382. ISSN 2079-4991. Available from DOI: 10.3390/nano11123382.

[35] ELAZAB, Hany A.; MOUSSA, Sherif; BRINKLEY, Kendra W.; GUPTON, B. Frank; EL-SHALL, M. Samy. The continuous synthesis of Pd supported on Fe3O4 nanoparticles: a highly effective and magnetic catalyst for CO oxidation. *Green Processing and Synthesis*. 2017, vol. 6, no. 4. ISSN 2191-9550, 2191-9542. ISSN 2191-9550, 2191-9542. Available from DOI: 10.1515/gps-2016-0168.

[36] LIU, Jixing et al. Deep Understanding of Strong Metal Interface Confinement: A Journey of Pd/FeO x Catalysts. *ACS Catalysis*. 2020, vol. 10, no. 15, pp. 8950–8959. ISSN 2155-5435, 2155-5435. ISSN 2155-5435, 2155-5435. Available from DOI: 10.1021/acscatal.0c01447.

[37] LI, Liang; LI, Gengnan; YUAN, Yuan; LI, Yongsheng. Facile synthesis of meso-structured Pd/FeO x and its highly catalytic performance for low temperature CO oxidation under ambient conditions. *RSC Advances*. 2015, vol. 5, no. 27, pp. 20650–20655. ISSN 2046-2069. Available from DOI: 10.1039/C5RA01118C.

[38] ZHOU, Qi-Lin. *Transition-metal catalysis and organocatalysis: where can progress be expected?* Wiley Online Library, 2016. No. 18.

[39] CORMA, Avelino; IBORRA, Sara; VELTY, Alexandra. Chemical Routes for the Transformation of Biomass into Chemicals. *Chemical Reviews*. 2007, vol. 107, no. 6, pp. 2411–2502. Available from DOI: 10.1021/cr050989d.

[40] NOTHLING, Mitchell D. et al. Simple Design of an Enzyme-Inspired Supported Catalyst Based on a Catalytic Triad. *Chem*. 2017, vol. 2, no. 5, pp. 732–745. Available from DOI: 10.1016/j.chempr.2017.04.004.

[41] ASTRUC, Didier. Introduction: Nanoparticles in Catalysis. *Chemical Reviews*. 2020, vol. 120, no. 2, pp. 461–463. Available from DOI: 10.1021/acs.chemrev.8b00696.

[42] WANG, Aiqin; LI, Jun; ZHANG, Tao. Heterogeneous single-atom catalysis. *Nature Reviews Chemistry*. 2018, vol. 2, no. 6, pp. 65–81. Available from DOI: 10.1038/s41570-018-0010-1.

[43] SHAN, Shiyao; LUO, Jin; YANG, Lefu; ZHONG, Chuan-Jian. Nanoalloy catalysts: structural and catalytic properties. *Catal. Sci. Technol.* 2014, vol. 4, no. 10, pp. 3570–3588. ISSN 2044-4753, 2044-4761. ISSN 2044-4753, 2044-4761. Available from DOI: 10.1039/C4CY00469H.

[44] MUNNIK, Peter; JONGH, Petra E. de; JONG, Krijn P. de. Recent Developments in the Synthesis of Supported Catalysts. *Chemical Reviews*. 2015, vol. 115, no. 14, pp. 6687–6718. ISSN 0009-2665, 1520-6890. ISSN 0009-2665, 1520-6890. Available from DOI: 10.1021/cr500486u.

[45] ARGYLE, Morris; BARTHOLOMEW, Calvin. Heterogeneous Catalyst Deactivation and Regeneration: A Review. *Catalysts*. 2015, vol. 5, no. 1, pp. 145–269. Available from DOI: 10.3390/catal5010145.

[46] PAN, Chun-Jern; TSAI, Meng-Che; SU, Wei-Nien; RICK, John; AKALEWORK, Nibret Gebeyehu; AGEGNEHU, Abiye Kebede; CHENG, Shou-Yi; HWANG, Bing-Joe. Tuning/exploiting Strong Metal-Support Interaction (SMSI) in Heterogeneous Catalysis. *Journal of the Taiwan Institute of Chemical Engineers*. 2017, vol. 74, pp. 154–186. ISSN 18761070. Available from DOI: 10.1016/j.jtice.2017.02.012.

[47] RO, Insoo; RESASCO, Joaquin; CHRISTOPHER, Phillip. Approaches for Understanding and Controlling Interfacial Effects in Oxide-Supported Metal Catalysts. *ACS Catalysis*. 2018, vol. 8, no. 8, pp. 7368–7387. ISSN 2155-5435, 2155-5435. ISSN 2155-5435, 2155-5435. Available from DOI: 10.1021/acscatal.8b02071.

[48] DEELEN, Tom W. van; HERNÁNDEZ MEJÍA, Carlos; JONG, Krijn P. de. Control of metal-support interactions in heterogeneous catalysts to enhance activity and selectivity. *Nature Catalysis*. 2019, vol. 2, no. 11, pp. 955–970. ISSN 2520-1158. Available from DOI: 10.1038/s41929-019-0364-x.

[49] SUCHORSKI, Yuri; KOZLOV, Sergey M.; BESPALOV, Ivan; DATLER, Martin; VOGEL, Diana; BUDINSKA, Zuzana; NEYMAN, Konstantin M.; RUPPRECHTER, Günther. The role of metal/oxide interfaces for long-range metal particle activation during CO oxidation. *Nature Materials*. 2018, vol. 17, no. 6, pp. 519–522. ISSN 1476-1122, 1476-4660. ISSN 1476-1122, 1476-4660. Available from DOI: 10.1038/s41563-018-0080-y.

[50] TAUSTER, S. J.; FUNG, S. C. Strong metal-support interactions: Occurrence among the binary oxides of groups IIA–VB. *Journal of Catalysis*. 1978, vol. 55, no. 1, pp. 29–35. ISSN 0021-9517. Available from DOI: 10.1016/0021-9517(78)90182-3.

[51] RUIZ PUIGDOLLERS, Antonio; SCHLEXER, Philomena; TOSONI, Sergio; PACCHIONI, Gianfranco. Increasing Oxide Reducibility: The Role of Metal/Oxide Interfaces in the Formation of Oxygen Vacancies. *ACS Catalysis*. 2017, vol. 7, no. 10, pp. 6493–6513. ISSN 2155-5435, 2155-5435. ISSN 2155-5435, 2155-5435. Available from DOI: 10.1021/acscatal.7b01913.

[52] PAN, Yanbo; SHEN, Xiaochen; YAO, Libo; BENTALIB, Abdulaziz; PENG, Zhenmeng. Active Sites in Heterogeneous Catalytic Reaction on Metal and Metal Oxide: Theory and Practice. *Catalysts*. 2018, vol. 8, no. 10, pp. 478. ISSN 2073-4344. Available from DOI: 10.3390/catal8100478.

[53] COQ, B. In: *Metal-Ligand Interactions in Chemistry, Physics and Biology*. Springer Netherlands, 2000, pp. 49–71. Available also from: https://doi.org/10.1007/978-94-011-4245-8_3.

[54] TAUSTER, S. J.; FUNG, S. C.; BAKER, R. T. K.; HORSLEY, J. A. Strong Interactions in Supported-Metal Catalysts. *Science*. 1981, vol. 211, no. 4487, pp. 1121–1125. ISSN 0036-8075, 1095-9203. ISSN 0036-8075, 1095-9203. Available from DOI: 10.1126/science.211.4487.1121.

[55] TAUSTER, S J; FUNG, S C; GARTEN, R L. Strong Metal-Support Interactions. Group 8 Noble Metals Supported on Ti02. *Journal of the American Chemical Society*. 1978, vol. 100, no. 1, pp. 170–175. Available from DOI: 10.1021/ja00469a029.

[56] O'CONNOR, Nolan J.; JONAYAT, A. S. M.; JANIK, Michael J.; SENFTLE, Thomas P. Interaction trends between single metal atoms and oxide supports identified with density functional theory and statistical learning. *Nature Catalysis*. 2018, vol. 1, no. 7, pp. 531–539. ISSN 2520-1158. Available from DOI: 10.1038/s41929-018-0094-5.

[57] FU, Qiang; WAGNER, Thomas; OLLIGES, Sven; CARSTANJEN, Heinz-Dieter. Metal−Oxide Interfacial Reactions: Encapsulation of Pd on TiO 2 (110). *The Journal of Physical Chemistry B*. 2005, vol. 109, no. 2, pp. 944–951. ISSN 1520-6106, 1520-5207. ISSN 1520-6106, 1520-5207. Available from DOI: 10.1021/jp046091u.

[58] WILLINGER, Marc G.; ZHANG, Wei; BONDARCHUK, Oleksandr; SHAIKHUTDINOV, Shamil; FREUND, Hans-Joachim; SCHLÖGL, Robert. A Case of Strong Metal-Support Interactions: Combining Advanced Microscopy and Model Systems to Elucidate the Atomic Structure of Interfaces. *Angewandte Chemie International Edition*. 2014, vol. 53, no. 23, pp. 5998–6001. ISSN 14337851. Available from DOI: 10.1002/anie.201400290.

[59] HORSLEY, J. A. A molecular orbital study of strong metal-support interaction between platinum and titanium dioxide. *Journal of the American Chemical Society*. 1979, vol. 101, no. 11, pp. 2870–2874. Available from DOI: 10.1021/ja00505a011.

[60] LOU, Y.; XU, J.; ZHANG, Y.; PAN, C.; DONG, Y.; ZHU, Y. Metal-support interaction for heterogeneous catalysis: from nanoparticles to single atoms. *Materials Today Nano*. 2020, vol. 12, pp. 100093. ISSN 25888420. Available from DOI: 10.1016/j.mtnano.2020.100093.

[61] GAO, Y.; LIANG, Y.; CHAMBERS, S. A. Thermal stability and the role of oxygen vacancy defects in strong metal support interaction — Pt on Nb-doped TiO2(100). *Surface Science*. 1996, vol. 365, no. 3, pp. 638–648. ISSN 0039-6028. Available from DOI: https://doi.org/10.1016/0039-6028(96)00763-7.

[62] DU, Xiaorui et al. Size-dependent strong metal-support interaction in TiO2 supported Au nanocatalysts. *Nature Communications*. 2020, vol. 11, no. 1, pp. 5811. ISSN 2041-1723. Available from DOI: 10.1038/s41467-020-19484-4.

[63] ZHANG, Yunshang; LIU, Jin-Xun; QIAN, Kun; JIA, Aiping; LI, Dan; SHI, Lei; HU, Jun; ZHU, Junfa; HUANG, Weixin. Structure Sensitivity of Au-TiO 2 Strong Metal–Support Interactions. *Angewandte Chemie International Edition*. 2021, vol. 60, no. 21, pp. 12074–12081. ISSN 1433-7851, 1521-3773. ISSN 1433-7851, 1521-3773. Available from DOI: 10.1002/anie.202101928.

[64] WU, Peiwen et al. Harnessing strong metal–support interactions via a reverse route. *Nature Communications*. 2020, vol. 11, no. 1, pp. 3042. ISSN 2041-1723. Available from DOI: 10.1038/s41467-020-16674-y.

[65] SHELDON, Roger A. Fundamentals of green chemistry: efficiency in reaction design. *Chemical Society Reviews*. 2012, vol. 41, no. 4, pp. 1437–1451.

[66] BARCIKOWSKI, Stephan; AMENDOLA, Vincenzo; LAU, Marcus; MARZUN, Galina; REHBOCK, Christoph; REICHENBERGER, Sven; ZHANG, Dongshi; GÖKCE, Bilal. *Handbook of Laser Synthesis & Processing of Colloids*. Second edition. 2019. Available from DOI: 10.17185/duepublico/70584.

[67] HUANG, Hongkun; LAI, Jiancheng; LU, Jian; LI, Zhenhua. Pulsed laser ablation of bulk target and particle products in liquid for nanomaterial fabrication. *AIP Advances*. 2019, vol. 9, no. 1, pp. 015307. ISSN 2158-3226. Available from DOI: 10.1063/1.5082695.

[68] JOHN, Mallory G.; TIBBETTS, Katharine Moore. One-step femtosecond laser ablation synthesis of sub-3 nm gold nanoparticles stabilized by silica. *Applied Surface Science*. 2019, vol. 475, pp. 1048–1057. ISSN 01694332. Available from DOI: 10.1016/j.apsusc.2019.01.042.

[69] BESNER, Sebastien; KABASHIN, Andrei V; WINNIK, Francoise M; MEUNIER, Michel. Synthesis of size-tunable polymer-protected gold nanoparticles by femtosecond laser-based ablation and seed growth. *The Journal of Physical Chemistry C*. 2009, vol. 113, no. 22, pp. 9526–9531.

[70] HASHIMOTO, Shuichi; WERNER, Daniel; UWADA, Takayuki. Studies on the interaction of pulsed lasers with plasmonic gold nanoparticles toward light manipulation, heat management, and nanofabrication. *Journal of Photochemistry and Photobiology C: Photochemistry Reviews*. 2012, vol. 13, no. 1, pp. 28–54.

[71] MAJUMDAR, Jyotsna Dutta; MANNA, Indranil. *Laser-assisted fabrication of materials*. Springer Science & Business Media, 2012.

[72] STAFE, Mihai; MARCU, Aurelian; PUSCAS, Niculae N. *Pulsed laser ablation of solids: basics, theory and applications*. Springer Science & Business Media, 2013.

[73] STREUBEL, René; BARCIKOWSKI, Stephan; GÖKCE, Bilal. Continuous multigram nanoparticle synthesis by high-power, high-repetition-rate ultrafast laser ablation in liquids. *Optics letters*. 2016, vol. 41, no. 7, pp. 1486–1489.

[74] TORRES MENDIETA, Rafael Omar et al. *Synthesis of colloidal nanomaterials through femtosecond laser ablation*. 2016. PhD thesis. Universitat Jaume I.

[75] MATSUMOTO, Ayumu et al. Transfer of the species dissolved in a liquid into laser ablation plasma: an approach using emission spectroscopy. *The Journal of Physical Chemistry C*. 2015, vol. 119, no. 47, pp. 26506–26511.

[76] HAVELKA, Bc Ondřej. Laser-generated synthesis of Pd-Ni nanoalloys usable as catalysts. 2021, pp. 109.

[77] CALLISTER, William D; RETHWISCH, David G. *Materials science and engineering: an introduction*. Wiley New York, 2018.

[78] HU, Sheng; TIAN, Mengkun; RIBEIRO, Erick L; DUSCHER, Gerd; MUKHERJEE, Dibyendu. Tandem laser ablation synthesis in solution-galvanic replacement reaction (LASiS-GRR) for the production of PtCo nanoalloys as oxygen reduction electrocatalysts. *Journal of Power Sources*. 2016, vol. 306, pp. 413–423.

[79] SHAHEEN, ME; GAGNON, JE; FRYER, BJ. Laser ablation of iron: a comparison between femtosecond and picosecond laser pulses. *Journal of Applied Physics*. 2013, vol. 114, no. 8, pp. 083110.

[80] LARA, Luciano R. S.; ZOTTIS, Alexandre D.; ELIAS, Welman C.; FAGGION, Deonildo; MADURO DE CAMPOS, Carlos Eduardo; ACUÑA, Jose Javier S.; DOMINGOS, Josiel B. The catalytic evaluation of in situ grown Pd nanoparticles on the surface of Fe 3 O 4@dextran particles in the p-nitrophenol reduction reaction. *RSC Advances*. 2015, vol. 5, no. 11, pp. 8289–8296. ISSN 2046-2069. Available from DOI: 10.1039/C4RA16440G.

[81] LIZ-MARZÃ¡N, Luis M.; CORREA-DUARTE, Miguel A.; PASTORIZA-SANTOS, Isabel; MULVANEY, Paul; UNG, Thearith; GIERSIG, Michael; KOTOV, Nicholas A. Chapter 5 - CORE-SHELL NANOPARTICLES AND ASSEMBLIES THEREOF. In: NALWA, Hari Singh (ed.). *Handbook of Surfaces and Interfaces of Materials*. Burlington: Academic Press, 2001, pp. 189–237. ISBN 978-0-12-513910-6. Available from DOI: https://doi.org/10.1016/B978-012513910-6/50038-4.

[82] KUMAR, Ajeet; DIXIT, Chandra Kumar. 3 - Methods for characterization ofÂ nanoparticles. In: NIMESH, Surendra; CHANDRA, Ramesh; GUPTA, Nidhi (eds.). *Advances in Nanomedicine for the Delivery of Therapeutic Nucleic Acids*. Woodhead Publishing, 2017, pp. 43–58. ISBN 978-0-08-100557-6. Available from DOI: https://doi.org/10.1016/B978-0-08-100557-6.00003-1.

[83] SCHIFFMAN, Peter; ROESKE, Sarah. Electron Microprobe Analysis of Minerals. In: MEYERS, Robert A. (ed.). *Encyclopedia of Physical Science and Technology (Third Edition)*. Third Edition. New York: Academic Press, 2003, pp. 293–306. ISBN 978-0-12-227410-7. Available from DOI: https://doi.org/10.1016/B0-12-227410-5/00211-8.

[84] BERTOTTI, Giorgio. Chapter 2 - Types of Hysteresis. In: BERTOTTI, Giorgio (ed.). *Hysteresis in Magnetism*. San Diego: Academic Press, 1998, pp. 31–70. Electromagnetism. ISBN 978-0-12-093270-2. Available from DOI: https://doi.org/10.1016/B978-012093270-2/50051-9.

[85] SHIRSATH, Sagar E.; JADHAV, Santosh S.; TOKSHA, B. G.; PATANGE, S. M.; JADHAV, K. M. Influence of Ce 4+ ions on the structural and magnetic properties of NiFe 2 O 4. *Journal of Applied Physics*. 2011, vol. 110, no. 1, pp. 013914. ISSN 0021-8979, 1089-7550. ISSN 0021-8979, 1089-7550. Available from DOI: 10.1063/1.3603004.

[86] VAINSHTEIN, Boris K; FRIDKIN, Vladimir M; INDENBOM, Vladimir L; INDENBOM, Vladimir L. *Modern Crystallography 2: Structure of crystals. Vol. 2*. Springer Science & Business Media, 2000.

[87] SAVIOT, Lucien. *Mie scattering by a core-shell particle - Lucien Saviot*. French National Centre for Scientific Research. Available also from: https://saviot.cnrs.fr/miecoat/index.en.html.

[88] SHIH, Cheng-Yu et al. Two mechanisms of nanoparticle generation in picosecond laser ablation in liquids: The origin of the bimodal size distribution. *Nanoscale*. 2018, vol. 10, no. 15, pp. 6900–6910.

[89] JOHNY, Jacob et al. Multidimensional thermally-induced transformation of nest-structured complex Au-Fe nanoalloys towards equilibrium. *Nano Research*. 2022, vol. 15, no. 1, pp. 581–592.

[90] ALSHARIF, Nizar B; MURÁTH, Szabolcs; KATANA, Bojana; SZILAGYI, Istvan. Composite materials based on heteroaggregated particles: Fundamentals and applications. *Advances in Colloid and Interface Science*. 2021, vol. 294, pp. 102456.

[91] MORROW, R; MCKENZIE, DR. The time–dependent development of electric double–layers in pure water at metal electrodes: the effect of an applied voltage on the local pH. *Proceedings of the Royal Society A: Mathematical, Physical and Engineering Sciences*. 2012, vol. 468, no. 2137, pp. 18–34.

[92] AMENDOLA, Vincenzo. Laser-Assisted Synthesis of Non-Equilibrium Nanoalloys. *ChemPhysChem*. 2021, vol. 22, no. 7, pp. 622–624. Available from DOI: https://doi.org/10.1002/cphc.202000987.

[93] QUAN, Zewei; WANG, Yuxuan; FANG, Jiye. High-index faceted noble metal nanocrystals. *Accounts of Chemical Research*. 2013, vol. 46, no. 2, pp. 191–202.

[94] CRANGLE, J; GOODMAN, G. M. The magnetization of pure iron and nickel. *Proceedings of the Royal Society of London. A. Mathematical and Physical Sciences*. 1971, vol. 321, no. 1547, pp. 477–491. ISSN 0080-4630. Available from DOI: 10.1098/rspa.1971.0044.

[95] *Chemistry of the Elements*. Elsevier Science & Technology Books, 1996. ISBN 9780080379418. Available also from: https://books.google.cz/books?id=z0a1AAAACAAJ.

[96] KING, R.B.; BURDETT, J.K.; CRABTREE, R.H.; LUKEHART, C.M.; SCOTT, R.A.; WELLS, R.L. *Encyclopedia of Inorganic Chemistry, 8 Volume Set*. Wiley, 1994. Encyclopedia of Inorganic Chemistry. ISBN 9780471936206. Available also from: https://books.google.cz/books?id=vijkzAEACAAJ.

[97] LAK, Aidin; KRAKEN, Mathias; LUDWIG, Frank; KORNOWSKI, Andreas; EBERBECK, Dietmar; SIEVERS, Sibylle; LITTERST, FJ; WELLER, Horst; SCHILLING, Meinhard. Size dependent structural and magnetic properties of FeO–Fe 3 O 4 nanoparticles. *Nanoscale*. 2013, vol. 5, no. 24, pp. 12286–12295.

[98] CVEK, Martin; TORRES-MENDIETA, Rafael; HAVELKA, Ondrej; URBANEK, Michal; PLACHY, Tomas; CERNIK, Miroslav. Laser-induced fragmentation of carbonyl iron as a clean method to enhance magnetorheological effect. *Journal of Cleaner Production*. 2020, vol. 254, pp. 120182.

[99] AGUILERA-DEL-TORO, Rodrigo Humberto; ALVARADO-LEYVA, Pedro Gilberto; VEGA, A. Uncovering the magnetic properties of the AgxNiy (x+ y= 55) nanoalloys in the whole composition range. *Journal of Magnetism and Magnetic Materials*. 2019, vol. 474, pp. 551–562.

[100] CAO, Shao-Wen; ZHU, Ying-Jie; CHANG, Jiang. Fe3O4 polyhedral nanoparticles with a high magnetization synthesized in mixed solvent ethylene glycol–water system. *New Journal of Chemistry*. 2008, vol. 32, no. 9, pp. 1526. ISSN 1144-0546, 1369-9261. ISSN 1144-0546, 1369-9261. Available from DOI: 10.1039/b719436f.

[101] GU, Shuo et al. Physical justification for negative remanent magnetization in homogeneous nanoparticles. *Scientific reports*. 2014, vol. 4, no. 1, pp. 1–7.

[102] TAKANASHI, Koki; KUROKAWA, H; FUJIMORI, H. A novel hysteresis loop and indirect exchange coupling in Co/Pt/Gd/Pt multilayer films. *Applied physics letters*. 1993, vol. 63, no. 11, pp. 1585–1587.

[103] DOS SANTOS, CA; RODMACQ, B. Inverted and crossed hysteresis loops in Ag/Ni multilayers. *Journal of magnetism and magnetic materials*. 1995, vol. 147, no. 3, pp. L250–L252.

[104] YAN, X; XU, Y. Negative remanence in magnetic nanostructures. *Journal of applied physics*. 1996, vol. 79, no. 8, pp. 6013–6015.

[105] DU, Yuanxin; SHENG, Hongting; ASTRUC, Didier; ZHU, Manzhou. Atomically precise noble metal nanoclusters as efficient catalysts: a bridge between structure and properties. *Chemical reviews*. 2019, vol. 120, no. 2, pp. 526–622.

A Appendix

Sample	d-spacing (Å)	Crystal and Miller indices (hkl)	ICDD file
pH 1	1.19 ± 0.03	FePd (311)	2–1440
	1.09 ± 0.04	FePd (113)	2–1440
	0.98 ± 0.01	FeO (122)	6–711
pH 3	1.12 ± 0.01	FePd (113)	2–1440
	1.21 ± 0.01	FeO (202)	6–711
	1.23 ± 0.01	FeO (202)	6–711
pH 3.6	1.11 ± 0.01	FePd (222)	2–1440
	1.26 ± 0.01	FeO (101)	6–711
	1.42 ± 0.01	Fe_3O_4 (440)	26–1136
pH 5	1.51 ± 0.01	FeO (110)	6–711
	1.24 ± 0.02	FeO (202)	6–711
	1.44 ± 0.02	Fe_3O_4 (440)	26–1136
pH 7	1.12 ± 0.01	FePd (222)	2–1440
	1.12 ± 0.01	FePd (222)	2–1440
	2.41 ± 0.01	FeO (111)	77–2355
pH 9	1.02 ± 0.01	FePd (312)	2–1440
	1.53 ± 0.01	FeO (104)	6–711
	0.98 ± 0.01	FeO (024)	6–711
pH 11	1.16 ± 0.01	FePd (311)	2–1440
	1.29 ± 0.01	FeO (104)	6–711
	1.06 ± 0.01	FeO (024)	6–711
pH 13	1.13 ± 0.01	FePd (113)	2–1440
	1.50 ± 0.01	FeO (104)	6–711
	1.29 ± 0.01	FeO (113)	6–711

Table A.1: List of crystallographic data belonging to HR-TEM analysis.

Sample	1/r (nm^{-1})	d-spacing (Å)	Crystal and Miller indices (hkl)	ICDD file
	5.15	1.93	Pd (200)	65–2867
	9.51	1.05	FePd (312)	2–1440
pH 1	8.50	1.17	FePd (311)	2–1440
	10.25	0.97	FeO (211)	6–711
	7.13	1.40	Fe_3O_4 (440)	26–1136
	9.13	1.09	FePd (222)	2–1440
	4.73	2.11	Fe (111)	52–513
	7.87	1.27	FeO (021)	6–711
	10.27	0.97	FeO (122)	6–711
pH 3	6.07	1.65	Fe_2O_3 (004)	47–1409
	6.80	1.47	Fe_2O_3 (220)	40–1139
	2.09	4.78	Fe_3O_4 (111)	79–416
	3.96	2.52	Fe_3O_4 (311)	74–748
	3.39	2.94	Fe_3O_4 (400)	76–955
	4.84	2.06	Fe (110)	89–4186
	6.07	1.65	Fe_2O_3 (004)	47–1409
pH 3.6	6.80	1.47	Fe_2O_3 (220)	40–1139
	2.09	4.78	Fe_2O_3 (110)	40–1139
	3.96	2.52	Fe_3O_4 (111)	74–748
	3.39	2.94	Fe_3O_4 (400)	76–955
	5.88	1.69	PdO_2 (211)/FeO (102)	34–1101/49–1447
	8.56	1.16	FePd (311)	2–1440
	9.85	1.01	FePd (312)	2–1440
pH 5	4.80	2.08	Fe (110)	89–4186
	3.87	2.58	FeO (002)	49–1447
	6.62	1.50	FeO (110)	6–711
	7.75	1.29	FeO (021)	6–711
	10.53	0.95	FeO (122)	6–711
	4.02	2.48	PdO_2 (111)/Fe_2O_3 (020)	65–5065/47–1409
	8.66	1.15	FePd (311)	2–1440
	4.85	2.06	Fe (110)	89–4186
	10.56	0.95	FeO (122)	6–711
pH 7	9.33	1.07	FeO (024)	6–711
	8.00	1.24	FeO (202)	6–711
	3.49	2.87	Fe_2O_3 (113)	40–1139
	6.95	1.43	Fe_3O_4 (440)	26–1136
	2.13	4.70	Fe_3O_4 (111)	79–416
	6.11	1.64	PdO (112)/Fe_2O_3 (004)	85–624/47–1409
	3.89	2.57	PdO (002)	75–200
	8.60	1.16	FePd (311)	2–1440
pH 9	9.69	1.03	FePd (312)	2–1440
	4.84	2.07	Fe (110)	89–4186
	10.09	0.99	FeO (122)	6–711
	6.79	1.47	Fe_3O_4 (440)	79–416
	1.92	5.20	PdO (001)	75–200
	8.56	1.16	FePd (311)	2–1440
	9.83	1.02	FePd (312)	2–1440
pH 11	4.91	2.03	Fe (110)	65–4899
	3.97	2.51	Fe_2O_3 (110)	79–7
	3.96	2.52	Fe_2O_3 (110)	79–7
	3.33	3.00	Fe_3O_4 (400)	76–955
	4.49	2.23	Pd (111)	65–2867
	8.56	1.16	FePd (311)	2–1440
	9.78	1.02	FePd (312)	2–1440
pH 13	4.92	2.02	Fe (110)	65–4899
	6.76	1.47	Fe_2O_3 (220)/Fe_3O_4 (440)	40–1139/79–416
	7.31	1.36	Fe_2O_3 (312)	47–1409
	3.99	2.50	Fe_2O_3 (110)	79–7
	3.38	2.95	Fe_3O_4 (400)	76–955

Table A.2: List of crystallographic data belonging to SAED analysis.